Neuron

Article

Distinct roles of prefrontal subregion feedback to the primary visual cortex across behavioral states

Graphical abstract

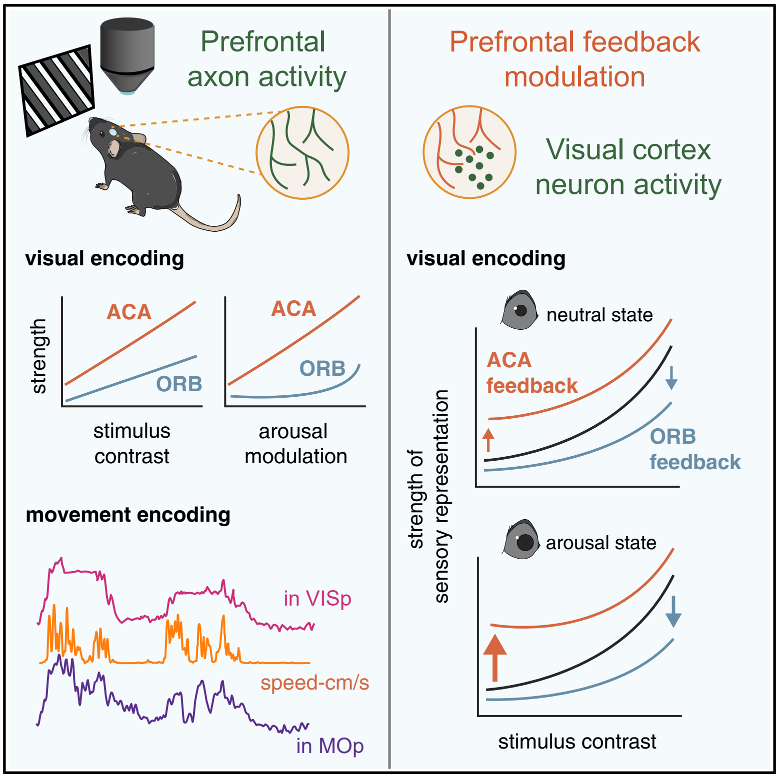

Highlights

- ACA and ORB projections show distinct laminar organization in VISp
- ACA axons encode stronger visual signals than ORB axons, both modulated by behavior
- ACA feedback enhances visual encoding in a manner dependent on arousal and contrast
- ORB feedback reduces high-contrast visual encoding in VISp neurons

Authors

Sofie Ährlund-Richter, Yuma Osako,
Kyle R. Jenks, Emma Odom,
Haoyang Huang, Don B. Arnold,
Mriganka Sur

Correspondence

sahrlund@mit.edu (S.Ä.-R.),
msur@mit.edu (M.S.)

In brief

Ährlund-Richter et al. show that in mice, discrete subregions of the prefrontal cortex send distinct feedback signals to the primary visual cortex. These pathways differentially modulate visual processing depending on behavioral state, revealing how higher-order cortical areas dynamically influence sensory representations to integrate perception with internal state.

Ährlund-Richter et al., 2026, Neuron *114*, 1–15
February 4, 2026
https://doi.org/10.1016/j.neuron.2025.10.037

CellPress

Please cite this article in press as: Ährlund-Richter et al., Distinct roles of prefrontal subregion feedback to the primary visual cortex across behavioral states, Neuron (2025), https://doi.org/10.1016/j.neuron.2025.10.037

Neuron

CellPress

Article

Distinct roles of prefrontal subregion feedback to the primary visual cortex across behavioral states

Sofie Ährlund-Richter,[1,*] Yuma Osako,[1] Kyle R. Jenks,[1] Emma Odom,[2] Haoyang Huang,[3] Don B. Arnold,[3] and Mriganka Sur[1,2,4,*]
[1]The Picower Institute for Learning and Memory, Massachusetts Institute of Technology, Cambridge, MA 02139, USA
[2]Department of Brain and Cognitive Sciences, Massachusetts Institute of Technology, Cambridge, MA 02139, USA
[3]Department of Biology, Division of Molecular and Computational Biology, Dornsife College, University of Southern California, Los Angeles, CA 90089, USA
[4]Lead contact
*Correspondence: sahrlund@mit.edu (S.Ä.-R.), msur@mit.edu (M.S.)
https://doi.org/10.1016/j.neuron.2025.10.037

SUMMARY

The mammalian prefrontal cortex (PFC) is thought to modulate cortical sensory processing during behavior through long-range feedback projections. Subregions of the PFC, such as the anterior cingulate cortex (ACA) and ventrolateral orbitofrontal cortex (ORB), exhibit unique patterns of connectivity that may confer distinct roles in feedback modulation of sensory information. Here, we combined axonal tracing, two-photon calcium imaging, and chemogenetic manipulations in mice to determine how projections from the ACA and ORB influence visual processing in the primary visual cortex (VISp). We found that ACA axons conveyed stronger visual-stimulus information than ORB axons, though both conveyed non-visual, behavior-related information. ACA input enhanced visual encoding in VISp neurons and scaled with behavioral arousal, whereas ORB input shaped behavior-related modulation but reduced high-contrast visual encoding. These results reveal distinct feedback roles of ACA and ORB projections, supporting the modular organization of PFC feedback modulation.

INTRODUCTION

A long-standing hypothesis of mammalian brain organization suggests that brain regions are hierarchically organized, with the relative order between two regions reflected in their laminar connectivity.[1,2] This bidirectional connectivity is proposed to allow higher-order regions to influence or modulate the activity of lower cortical regions to optimize sensory information processing.[3,4] Large-scale brain mapping identifies the prefrontal cortex (PFC) and its subregions at the top of this hierarchy in mice, with the majority of PFC efferents classified as feedback projections.[5] PFC subregions project to both shared and unique cortical targets,[6,7] forming a comprehensive pattern of axonal innervation across the cortex.[8,9] This anatomical organization ideally positions the PFC to guide or modulate cortex-wide activity and thereby shape information processing and ultimately behavior. Indeed, perturbation of PFC activity has been observed to not only disrupt cortex-wide activity dynamics but also behavioral performance.[10,11] However, it remains unclear whether this heterogeneity of projection targets across PFC subregions corresponds to equally diverse functional feedback or if the PFC provides a more uniform, brain-state-dependent modulation across the cortex.

A key feedback circuit, present across mammalian species and well-studied in rodent models, is the projection from the PFC to the primary visual cortex (VISp).[12,13] In the mouse, the VISp is targeted by two distinct PFC subregions, the anterior cingulate cortex (ACA) and the ventrolateral orbitofrontal cortex (ORB).[6,14–16] Previous studies suggest a functional dichotomy between ACA and ORB feedback during visually guided tasks: ACA enhances the encoding of behaviorally relevant stimuli, facilitating selective attention,[17] whereas ORB filters out irrelevant visual inputs to support associative learning.[18] Two opposing local inhibitory motifs have also been described, with ACA axons recruiting vasoactive intestinal peptide (VIP)$^+$ interneurons to amplify VISp responses[17] and ORB axons recruiting SST$^+$ interneurons to suppress them.[18] These studies ostensibly offer a circuit-based mechanism for how feedback modulation could alter the task-dependent representation of visual stimuli, but they also mask our limited insight into the nature of information that ACA and ORB inputs actually convey to VISp. Apart from invoking differences in connectivity from ACA and ORB to two VISp inhibitory neuron classes,[17,18] which represent only a subset of their targets[16] (also this study), the activation of these feedback projections by optogenetics drives an artificial pattern

Please cite this article in press as: Ährlund-Richter et al., Distinct roles of prefrontal subregion feedback to the primary visual cortex across behavioral states, Neuron (2025), https://doi.org/10.1016/j.neuron.2025.10.037

of activity with debatable physiological relevance to the activity driven by natural behavioral states. Other functions ascribed to top-down projections from prefrontal to sensory cortices, such as predictive signaling,[19,20] similarly invoke an assumption that such modulatory signals exist in top-down projections, without knowledge of what exactly the signals might be.

We reasoned that a careful, unbiased description of the responses of ACA and ORB inputs to VISp in freely observing and locomoting mice during natural behavioral states would provide a compendium of properties that would be important for all future studies of top-down influences of PFC on VISp or other targets. Indeed, recent studies on the complexity of PFC axonal innervation reveal that both ACA and ORB comprise neurons projecting exclusively to visual cortex and others with collateral projections extending to additional cortical regions, such as primary motor cortex (MOp).[8,9] This discovery has created additional gaps in our understanding of PFC feedback. To what extent do target regions receive similar feedback from the PFC, or is feedback tailored for each target region?

Imaging the activity of ACA and ORB axons in both the VISp and the MOp, we observed a stronger representation of visual information in ACA axons in comparison to ORB axons and a stronger representation of movement velocity in axons projecting to the MOp in comparison to the VISp. ACA axon activity scaled with arousal. Imaging of the same VISp neurons with and without chemogenetic suppression of ACA or ORB feedback revealed that the ACA and ORB play complementary roles: ACA inputs enhance visual encoding in relation to arousal, whereas ORB inputs are strongly driven by high arousal and movement, even at the expense of visual encoding in the VISp. Our data support a model of PFC feedback that is specialized at both the level of PFC subregions and their targets, enabling each region to selectively shape target-specific cortical activity rather than modulating it globally.

RESULTS

Cortical targets of ACA and ORB projection neurons

To characterize feedback projections from the ACA and ventrolateral ORB, we mapped their axonal density and identified postsynaptic targets across cortical regions and layers, focusing on the VISp and MOp. To confirm stereotaxic targeting of VISp-projecting neurons, we injected retroAAV-hSyn-GFP into VISp, which produced dense labeling in ACA and ORB consistent with prior studies[21] (Figures S1A–S1D). For cortex-wide mapping, AAV-CAG-tdTomato and AAV-CAG-GFP were unilaterally injected into ACA and ORB, respectively (Figures 1A and S1E). Coronal sections (50 μm) were aligned to the Allen Reference Atlas (ARA)[22] using a modified version of the WholeBrainSuite in R,[23] generating density (μm^2 axon/μm^2 area) estimates (Figure 1B). ACA and ORB projection neurons broadly targeted overlapping cortical areas, e.g., visual, motor, somatosensory, and auditory cortices, as previously described,[7] though projection density differed between the two PFC sources (Figures 1C and S1F–S1I). Both regions sent dense axonal projections to retrosplenial (RSP) and visual cortices, with ACA innervating both dorsal and ventral RSP, while ORB projections were largely confined to dorsal RSP. Within the visual cortex, both regions innervated all major subregions, with the highest density in the anteromedial visual area (VISam), spanning all layers (Figures 1D–1F). In other visual areas (anterolateral visual area [VISal], lateral visual area [VISl], VISp, posterolateral visual area [VISpl], and posteromedial visual area [VISpm]), ACA axons primarily targeted layers 1 and 6, whereas ORB axons were enriched in layers 1 and 5 (Figures 1F and S1J). Although layer-specific ACA and ORB innervation of VISp has been reported,[16] our cortex-wide mapping revealed that this laminar segregation extends across all visual areas but is less distinct in other sensory cortices or MOp (Figures S1F and S1H).

To identify postsynaptic targets of ACA and ORB projections in VISp and MOp, we used the anterograde transsynaptic label based on antibody-like sensor (ATLAS) system,[24] injecting into ACA or ORB to deliver Cre to downstream neurons. Subsequent AAV-DIO-tdTomato injections into VISp and MOp labeled neurons monosynaptically targeted by ACA or ORB projections (Figures 1G and S1K). This approach was particularly valuable as long-range PFC inputs target dendrites in superficial layers, while their postsynaptic partners may reside in deeper layers, such as layer 5.[25] Thus, axonal projection density alone does not necessarily predict the laminar location of postsynaptic cell bodies. Immunohistochemical analysis of somatostatin (SST), parvalbumin (PV), and VIP interneurons showed that both excitatory (triple-negative) and inhibitory neurons across all layers of VISp and MOp are monosynaptically targeted by ACA and ORB axons (Figures 1H–1J and S1L).

Overall, we found that long-range projections of ACA and ORB target discrete layers in the visual cortex and have access to both excitatory and inhibitory local microcircuitry. This anatomical difference in connectivity between the two PFC regions thus suggests that differences may exist in their influences on VISp activity.

ACA axons have stronger visually driven activity that scales with contrast, compared with ORB axons

To examine visually driven activity in ACA and ORB axons projecting to VISp, we injected AAV-axon-GCaMP6s into either PFC region and performed 2-photon calcium imaging in VISp (10–150 μm depth). As PFC projection neurons form extensive collaterals across the cortex,[9] ACA and ORB axonal calcium activity in the MOp was also recorded in separate cohorts of mice to compare modulatory activity putatively transmitted on a cortex-wide scale to modulatory activity unique to the VISp or MOp. Cranial windows were implanted over VISp or MOp, and axonal activity was recorded in layer 1 and superficial layer 2 (Figures 2A–2C). Once habituated, awake behaving mice were free to run on a running wheel while visual stimuli were presented to the contralateral eye (in relation to the cranial window; Figure 2D). Each mouse underwent two daily stimulus sessions: (1) drifting gratings of eight directions at three contrasts and (2) five natural movies at three contrasts (see STAR Methods for details). In some sessions, uncued air puffs to the ipsilateral eye and face were delivered in alternating trial blocks to evoke arousal. Active axonal segments (regions of interests [ROIs]) were identified using Suite2p.[26] To prevent oversampling of correlated segments from the same axonal branch, identified ROIs were clustered based on activity correlation measurements and averaged together to represent one axonal branch[27] (see STAR Methods). An axon was considered visually

Please cite this article in press as: Ährlund-Richter et al., Distinct roles of prefrontal subregion feedback to the primary visual cortex across behavioral states, Neuron (2025), https://doi.org/10.1016/j.neuron.2025.10.037

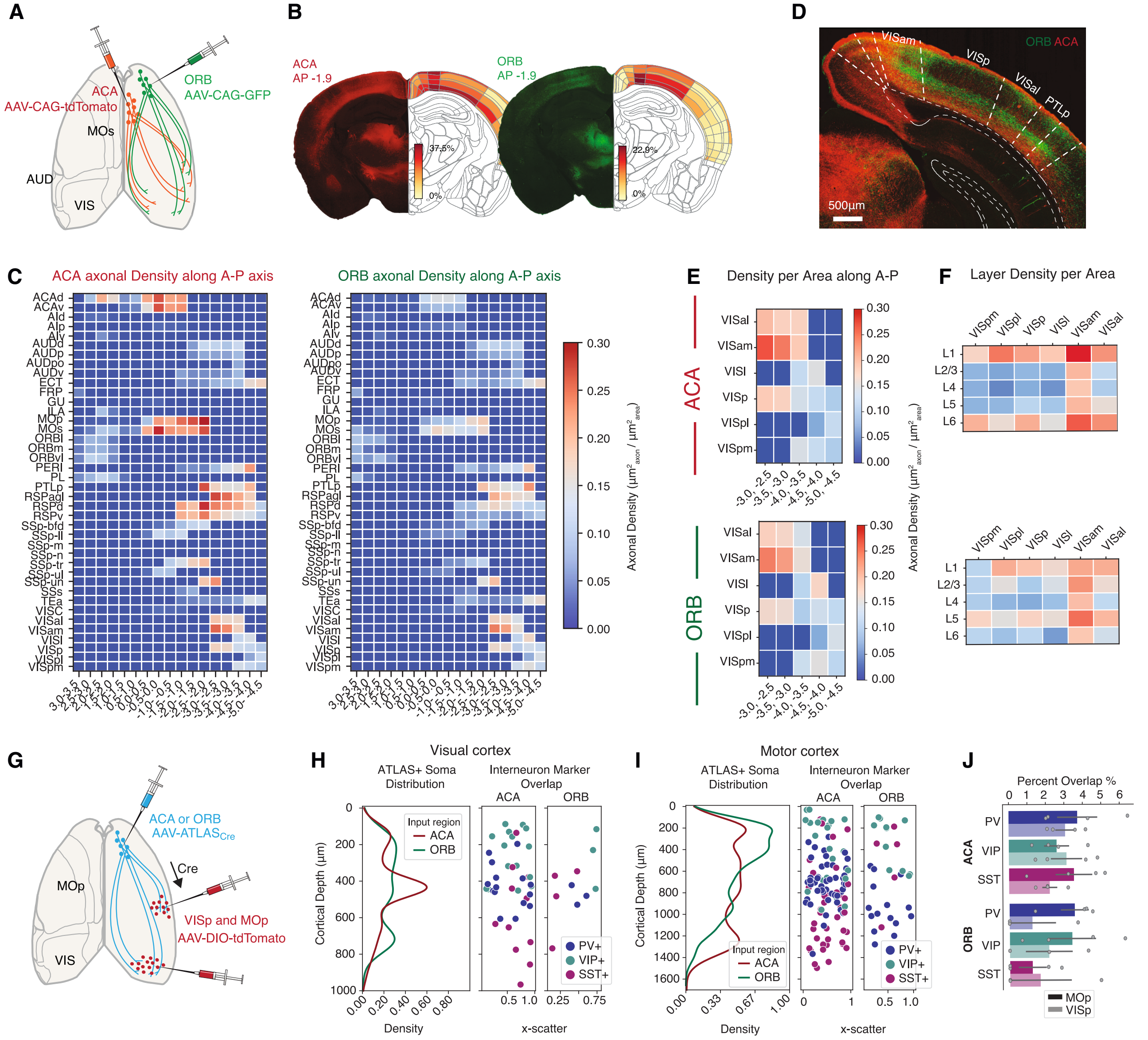

Figure 1. Axonal projections from the ACA and the ORB innervate discrete layers of the VISp and adjacent regions and target diverse neuron classes

(A) Experimental strategy. AAV-CAG-tdTomato and AAV-CAG-GFP were unilaterally injected into the ACA and ORB, respectively.

(B) Example brain section (green and red channels split) mapped to the Allen Brain Atlas, showing axonal density across cortical regions and layers.

(C) Average axonal density per cortical region and anterior-posterior (A-P) coordinate bin across all mice ($n = 4$, 67 ± 20 sections per animal) from the ACA (left) and ORB (right). Abbreviations from the Allen Brain Institute mouse brain reference atlas.

(D) Example image of VISp and surrounding visual regions showing ORB (green) and ACA (red) axonal innervation targeting superficial and deep layers (split channels in Figure S1).

(E) Average axonal density of ACA (top) and ORB (bottom) projections in visual regions along the A-P axis ($n = 4$ mice). VISal, anterolateral visual area; VISam, anteromedial visual area; VISl, lateral visual area; VISpl, posterolateral visual area; VISpm, posteromedial visual area.

(F) Axonal density per cortical layer for all visual regions ($n = 4$ mice).

(G) Experimental strategy. AAV-ATLASCre was unilaterally injected into the ACA or ORB, followed by AAV-DIO-tdTomato injection into the VISp and MOp.

(H) Left: kernel density estimate (KDE) of tdTomato+ neurons monosynaptically targeted by ACA (red) or ORB (green) along visual cortex depth. Right: tdTomato+ neurons overlapping with PV (blue), SST (purple), or VIP (green) labeling along cortex depth, all sections aligned along the A-P axis. ACA: $n = 4$ mice; MOp, 32 sections; VISp, 31 sections. ORB: $n = 3$ mice; MOp, 30 sections; VISp, 15 sections.

(I) Left: KDE of tdTomato+ neurons targeted by ACA (red) or ORB (green) along motor cortex depth. Right: overlap with PV (blue), SST (purple), or VIP (green) labeling, all sections aligned along the A-P axis. ACA: $n = 4$ mice; MOp, 32 sections; VISp, 31 sections. ORB: $n = 3$ mice; MOp, 30 sections; VISp, 15 sections.

(J) Percentage overlap of tdTomato+ neurons with PV (blue), SST (purple), or VIP (green) in MOp (dark) and VISp (light). ACA: $n = 4$ mice; MOp, 32 sections; VISp, 31 sections. ORB: $n = 3$ mice; MOp, 30 sections; VISp, 15 sections. Error bars: SEM; dots represent individual animals.

See also Figure S1.

Please cite this article in press as: Ährlund-Richter et al., Distinct roles of prefrontal subregion feedback to the primary visual cortex across behavioral states, Neuron (2025), https://doi.org/10.1016/j.neuron.2025.10.037

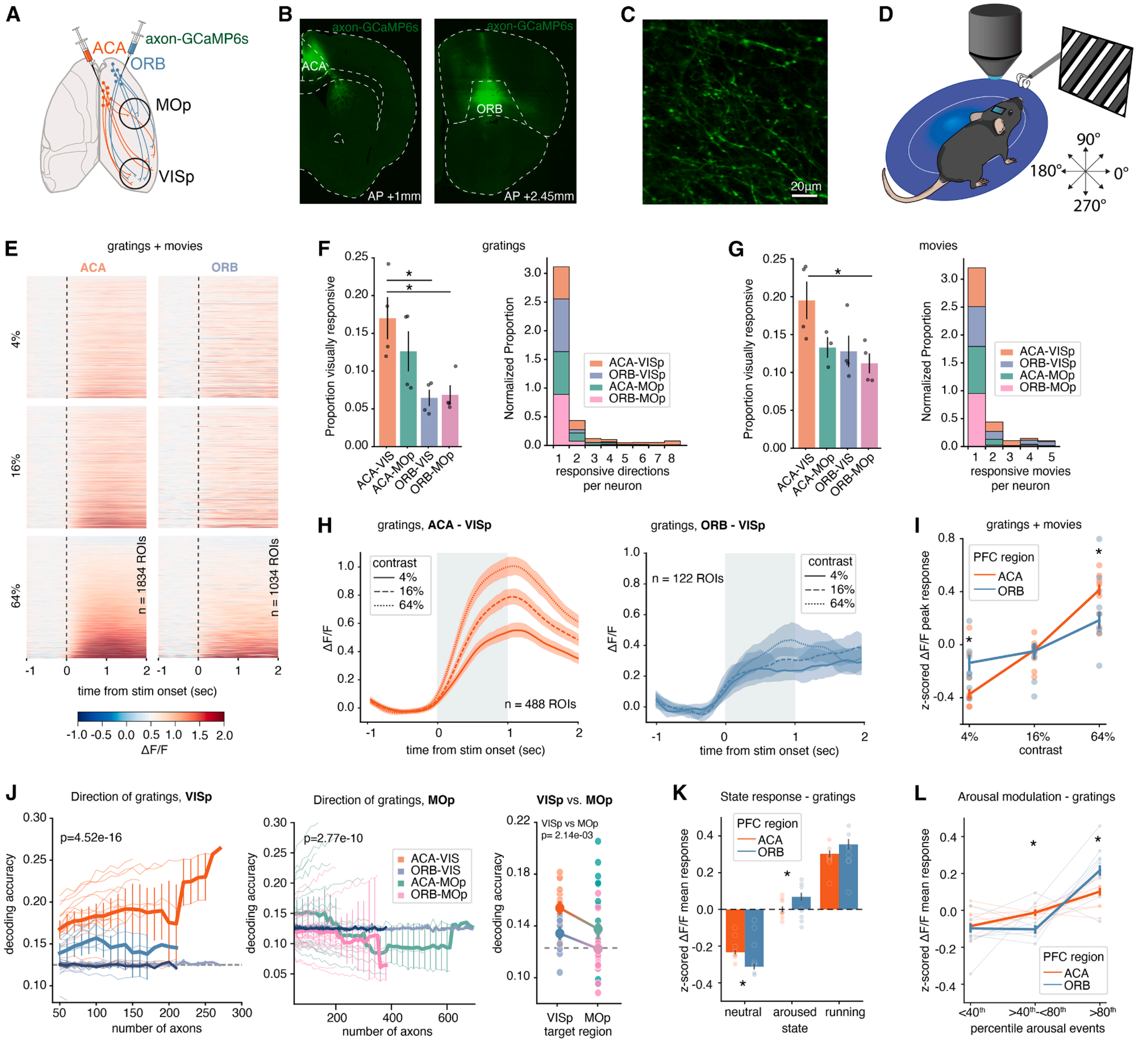

Figure 2. ACA and ORB axonal activity in VISp and MOp convey visually driven information that is differently modulated by behavioral state

(A) Experimental strategy. Axon-targeting GCaMP6s (AAV-hSyn-axon-GCaMP6s) were injected unilaterally into either the ACA or ORB, and a cranial window was implanted above VISp or MOp.

(B) Representative viral injection sites in the ACA (left) and ORB (right). Replicated in $n = 4$ ACA-VISp, 4 ORB-VISp, 4 ACA-MOp, and 4 ORB-MOp mice.

(C) Example 2-photon field of view of ACA axons in VISp.

(D) Schematic of behavioral setup.

(E) Heatmap of visually responsive axons in MOp and VISp from ORB (left) or ACA (right). Average responses across ten trials for each contrast and direction/movie; all directions/movies included. Axons sorted by peak response amplitude to 64% contrast. ACA-VISp/MOp: 1,834 axons from 8 mice; ORB-VISp/MOp: 1,034 axons from 8 mice.

(F) Proportion of visually responsive axons to gratings (left) from the ACA or the ORB in the VISp or the MOp. Bars: mean of proportions; error bars: SEM; dots: individual animals. ACA-VISp vs. ORB-VISp: $p = 0.0345$; ACA-VISp vs. ORB-MOp: $p = 0.0231$ (one-way ANOVA with Tukey's post hoc test). Selectivity of visually responsive axons (right) shown as the normalized distribution of the number of directions to which each axon responded significantly.

(G) Proportion of visually responsive axons to movies (left) from the ACA or the ORB in the VISp or the MOp. Bars: mean of proportions; error bars: SEM; dots: individual animals. ACA-VISp vs. ORB-MOp: $p = 0.0432$ (one-way ANOVA with Tukey's post hoc test). Selectivity of visually responsive axons (right) shown as the normalized distribution of the number of movies to which each axon responded significantly.

(H) Averaged population responses of visually responsive axons with increased ΔF/F to gratings, plotted per contrast (left: ACA-VISp; right: ORB-VISp). ACA-VISp: 488 axons (4 mice); ORB-VISp: 122 axons (4 mice). Solid line: mean; shaded area: 95% confidence interval (CI).

(I) Standardized ΔF/F peak responses during stimulus on-time plotted per contrast. Visually responsive axons in the VISp and MOp with significant ΔF/F increase included. ΔF/F peaks were Z scored across all trials and contrasts for each axon (negative = below-average; positive = above-average amplitudes).

(legend continued on next page)

responsive if mean ΔF/F during stimulus presentation differed significantly from baseline (1 s pre-stimulus) for at least one unique stimulus (Student's paired *t* test, p value < 0.00625 for gratings, and p value < 0.001 for movies; Figure 2E).

ACA axons in VISp showed the highest proportion of visually responsive axons (gratings: 0.17 ± 0.03, 122 ± 14 axons; movies: 0.19 ± 0.02, 125 ± 9 axons; mean ± SEM), followed by ACA axons in MOp (gratings: 0.13 ± 0.03, 182 ± 57; movies: 0.13 ± 0.01, 119 ± 56; n = 4 mice). ORB axons were overall significantly less responsive than ACA axons in VISp (VISp: gratings = 0.06 ± 0.01 (31 ± 25 axons), movies = 0.13 ± 0.02 (42 ± 29); MOp: gratings = 0.07 ± 0.01 (84 ± 17), movies = 0.11 ± 0.01 (123 ± 41); n = 4 mice; Figures 2F and 2G). The majority of visually responsive ACA and ORB axons increased activity during visual stimulation (Figures S3A and S3B) and were selective for one specific grating direction or movie (Figures 2F and 2G). The responses of excitatory neurons in visual areas scale with visual contrast.[28] Similarly, visually responsive ACA axons in both VISp and MOp exhibited mean and peak response amplitudes that increased with stimulus contrast, whereas responsive ORB axons showed little contrast dependence (Figures 2H and S2). ACA axons displayed a greater difference between responses to high- and low-contrast stimuli than did ORB axons for both drifting gratings and natural movies (Figure 2I).

Although a smaller fraction of ORB axons were visually responsive compared with ACA axons, we tested whether, as a population, they could carry comparable information about stimulus identity. A linear support vector machine (SVM) was trained to decode stimulus identity from mean ΔF/F responses of ACA and ORB axons in VISp. The decoder trained on ACA axon activity outperformed the decoder trained on ORB responses (Figure 2J, left). While mean response-based decoding for movie identity did not differ, temporal decoding accuracy was higher for ACA axons across both movies and gratings in VISp (Figures S3C and S3D). Comparing projections across targets revealed stronger visual information in PFC axons from both subregions to VISp than to MOp (Figure 2J). Thus, visual information was encoded more robustly in ACA than ORB axons, but both subregions transmitted stronger visual signals to VISp than MOp.

Visual responses of VISp neurons change in relation to the behavioral state of the animal,[29] and top-down projections are known to carry non-visual information to sensory areas.[19,30] We monitored pupil diameter and locomotion to classify each trial into three behavioral states: aroused (>80th percentile pupil size or arousal events), running (>80th percentile speed), and neutral (stationary, <20th percentile arousal; see STAR Methods). Mean response amplitudes of ACA and ORB axons to their preferred stimuli were modulated by state, with higher normalized responses during aroused or running trials compared with neutral ones (Figures 2K, S3E, and S3F). Notably, ORB axons exhibited larger amplitude shifts between neutral and aroused states, showing lower responses than ACA axons during neutral trials but higher during aroused ones (Figure 2K). Under moderate arousal (>40th <80th percentile), ACA axon responses scaled more gradually with arousal, whereas ORB responses increased sharply only at high arousal (Figure 2L).

To summarize, ACA axon visual response amplitudes were more reflective of both the contrast of the visual stimuli and level of arousal, suggesting a modulatory effect onto VISp activity incorporating both visual-stimulus information and a continuum of arousal state. ORB axon visual responses did not discriminate direction and contrast as well but instead reflected a discrete behavioral state of high arousal. Comparing ACA and ORB input to VISp vs. MOp revealed that while discrete traits such as contrast encoding and behavioral state modulation of visual responses were still preserved in ACA and ORB axon activity within MOp, the population-level strength of visual information was weaker in PFC projections to MOp. Thus, PFC regions preferentially send visual information to VISp compared with MOp.

Visual information in ACA axons scales with arousal level

To test whether visual information encoded by PFC axons depends on behavioral state, we trained an SVM across all trials and evaluated single-trial decoding accuracy by state. In VISp, ACA axons decoded stimulus identity significantly better during running and arousal trials than during neutral ones (Figures 3A and 3B). ORB axons showed a similar but smaller improvement

---

ACA-VISp/MOp: 1,854 axons; ORB-VISp/MOp: 1,053 axons. Solid line: mean standardized ΔF/F peak responses; error bars: 95% CI; dots: individual animals. ACA vs. ORB: 4% p = 0.001; 64% p = 0.001 (one-way ANOVA with Tukey's post hoc test).

(J) Decoding accuracy of an SVM classifier trained on ΔF/F responses of ACA (orange/green) or ORB (blue/pink) axons in the VISp (left) or MOp (middle). Shuffled controls are shown in gray. Solid line: mean; error bars: 95% CI (omitted when only one session contributed); dashed line: chance level. p values from two-way ANCOVA to examine the effects of subset (number of axons) and PFC subregion (ACA vs. ORB) on the accuracy of decoding. The model included interaction terms to explore if the effect of subset on accuracy varies by group and data/shuffled data. VISp-ACA vs. ORB: $p = 4.52 \times 10^{-16}$; MOp-ACA vs. ORB: $p = 2.77 \times 10^{-10}$. Right: average decoding accuracy across sessions in VISp and MOp for both subregions. Each dot represents one session; colors distinguish ACA-MOp, ACA-VISp, ORB-MOp, and ORB-VISp. Independent-samples *t* test between MOp and VISp: $p = 2.14 \times 10^{-3}$. VISp-ACA: 18 fields of view (FOVs, 4 mice); ORB: 12 FOVs (4 mice). MOp-ACA: 21 FOVs (4 mice); ORB: 26 FOVs (4 mice).

(K) Standardized ΔF/F mean responses during stimulus on-time of visually responsive axons in the VISp and MOp per behavioral state. Behavioral states: > 80th percentile per session (running, movement, pupil size, arousal) and < 80th percentile, neutral. Only directions with all three states represented were included. ΔF/F mean responses are *Z* scored across each axon. Bars: mean standardized ΔF/F responses; error bars: 95% CI; dots: individual animals. ACA vs. ORB: neutral p < 0.001; aroused p < 0.001 (one-way ANOVA with Tukey's post hoc test).

(L) Standardized ΔF/F mean responses during stimulus on-time per arousal state. States defined by pupil size *Z* score: < 40th (neutral), 40–80th, and > 80th percentile. Axons were included if each arousal state contained at least one presentation. ΔF/F mean responses are *Z* scored across each axon. Solid line: mean standardized ΔF/F responses; error bars: 95% CI; thin lines and dots: individual animals. ACA vs. ORB: 40–80th p < 0.001; > 80th p = 0.0061 (one-way ANOVA with Tukey's post hoc test).

See also Figures S2 and S3.

Please cite this article in press as: Ährlund-Richter et al., Distinct roles of prefrontal subregion feedback to the primary visual cortex across behavioral states, Neuron (2025), https://doi.org/10.1016/j.neuron.2025.10.037

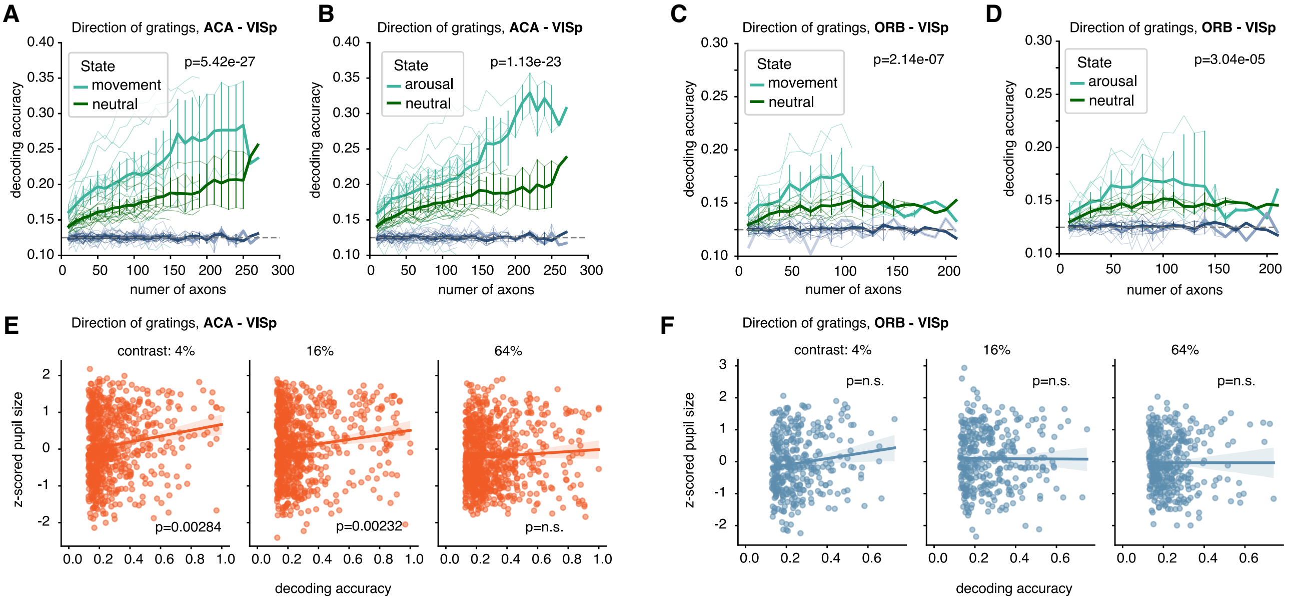

Figure 3. Decoding accuracy of visual information scales with arousal level in ACA axons

(A) Decoding accuracy of an SVM classifier trained on ACA axonal responses to drifting gratings (mean ΔF/F during stimulus on-time) in the VISp and tested trial-by-trial. Single-trial decoding accuracy, averaged per session, is plotted for movement (light green) and neutral (dark green) trials. *p* value from the variability in accuracy explained by group (movement vs. neutral): 5.42×10^{-27}. 18 FOVs across 4 mice. 855 running trials, 3,420 neutral trials.

(B) Decoding accuracy of an SVM classifier trained on ACA axonal responses to drifting gratings (mean ΔF/F during stimulus on-time) in the VISp and tested trial-by-trial. Single-trial decoding accuracy, averaged per session, is plotted for arousal (light green) and neutral (dark green) trials. *p* value from the variability in accuracy explained by group (arousal vs. neutral): 1.13×10^{-23}. 18 FOVs across 4 mice. 1,036 arousal trials, 3,455 neutral trials.

(C) Decoding accuracy of an SVM classifier trained on ORB axonal responses to drifting gratings (mean ΔF/F during stimulus on-time) in the VISp and tested trial-by-trial. Single-trial decoding accuracy, averaged per session, is plotted for movement (light green) and neutral (dark green) trials. *p* value from the variability in accuracy explained by group (movement vs. neutral): 2.14×10^{-7}. 9 fields of view across 4 mice. 432 running trials, 1,728 neutral trials.

(D) Decoding accuracy of an SVM classifier trained on ORB axonal responses to drifting gratings (mean ΔF/F during stimulus on-time) in the VISp and tested trial-by-trial. Single-trial decoding accuracy, averaged per session, is plotted for arousal (light green) and neutral (dark green) trials. *p* value from the variability in accuracy explained by group (arousal vs. neutral): 3.04×10^{-5}. 9 fields of view across 4 mice. 432 arousal trials, 1,728 neutral trials.

(A–D) Decoding accuracy of shuffled ACA/ORB axonal responses (movement/arousal, light gray; neutral, dark gray) plotted for comparison. Speed/pupil value per trial is the average −1 s before, during, and after visual-stimulus onset. Behavioral state was classified as > 80th percentile trials per session (running speed, movement; pupil size, arousal; < 80th percentile, neutral). Thick solid line: mean accuracy across sessions; error bars: 95% CI (omitted when only one session contributed); thin lines: individual sessions; dashed line: chance level. *p* values from two-way ANCOVA examining the effects of subset (number of axons) and behavioral state on decoding accuracy. The model included interaction terms to test whether the effect of subset size on accuracy varied by group and data/shuffled data.

(E) Linear-regression lines fit to *Z* scored pupil size and decoding accuracy per trial, per contrast, for ACA axons to drifting gratings. Slopes and significance levels determined using ordinary least square (OLS) regression. Dots: single trials; shaded area: 95% CI. Number of trials per contrast: 4% $n = 710$; 16% $n = 757$; 64% $n = 834$. *p* value and slope per contrast: 4% slope = −0.469, $p = 0.0028$; 16% slope = −0.422, $p = 0.0023$; 64% slope = −0.422, $p = 0.0023$.

(F) Linear-regression lines fit to *Z* scored pupil size and decoding accuracy per trial, per contrast, for ORB axons to drifting gratings. Slopes and significance levels determined using OLS regression. Dots: single trials; shaded area: 95% CI. Number of trials per contrast: 4% $n = 352$; 16% $n = 348$; 64% $n = 364$. *p* value and slope per contrast: 4% slope = −2.197, $p = 0.148$; 16% slope = −0.348, $p = 0.795$; 64% slope = −1.934, $p = 0.180$.

for visual-stimulus direction (Figures 3C and 3D). To assess whether decoding scaled continuously with arousal, we correlated decoding accuracy with *Z* scored pupil size on a trial-by-trial basis. ACA axon decoding accuracy increased linearly with pupil size, but this relationship was significant only for low-contrast stimuli (Figure 3E) and absent in ORB axons (Figure 3F).

These results suggest that ACA axons provide the VISp with a representation of low-contrast (low-evidence) visual stimuli that scales with arousal, whereas ORB axons' representation of visual stimuli is strengthened during high levels of arousal but without a continuous modulation related to arousal level.

ACA and ORB axonal activity differentially reflect behavioral state across VISp and MOp

Given that PFC axons showed state-dependent modulation of visual responses (Figure 2), we next addressed how ACA and ORB axons represent behavioral variables on a population level. Most ACA and ORB axon activity correlated significantly with pupil diameter, facial motion, and locomotion in both VISp and MOp (Figures S4A–S4D). As ACA and ORB visual responses scaled differently with pupil dilation, we compared how axonal activity related to discrete behavioral metrics (running speed, face velocity, and pupil size) vs. binary state measures (moving/stationary and dilated/constricted) and

Please cite this article in press as: Ährlund-Richter et al., Distinct roles of prefrontal subregion feedback to the primary visual cortex across behavioral states, Neuron (2025), https://doi.org/10.1016/j.neuron.2025.10.037

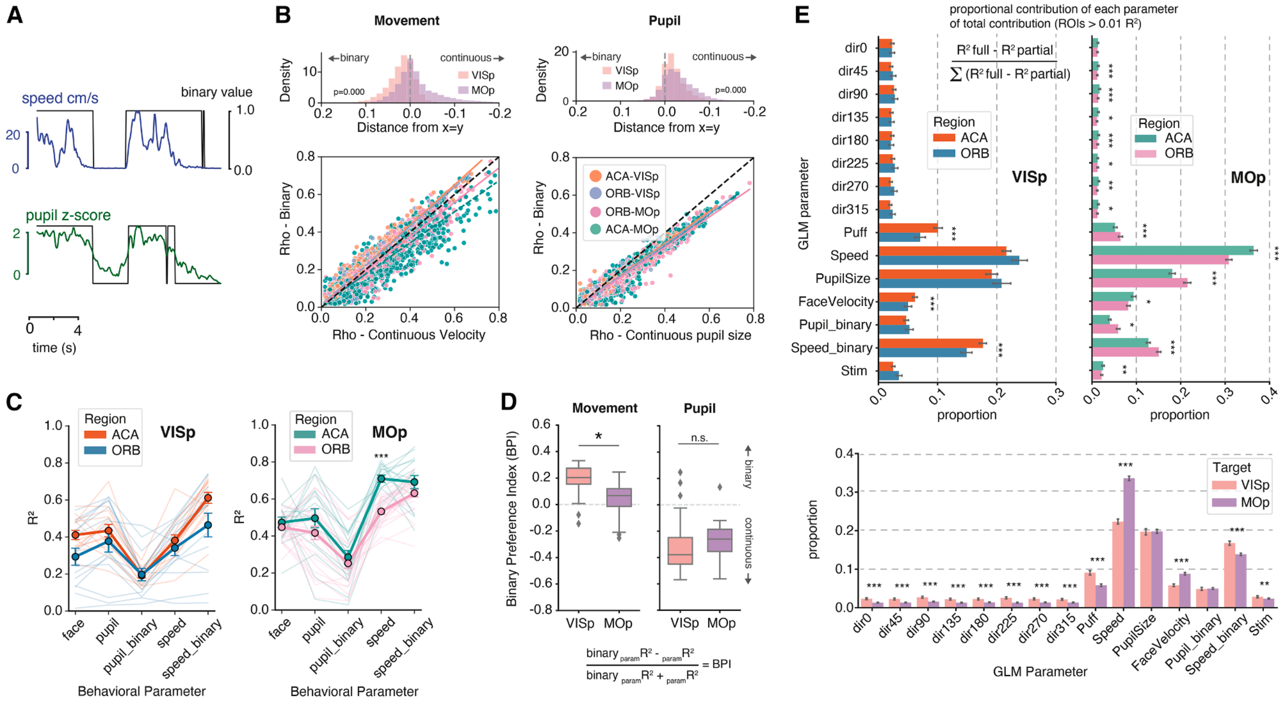

$$\frac{\text{binary}_{\text{param}}R^2 - {}_{\text{param}}R^2}{\text{binary}_{\text{param}}R^2 + {}_{\text{param}}R^2} = \text{BPI}$$

Figure 4. ACA and ORB axonal activity in the VISp are modulated by pupil size and a binary movement state

(A) Example trace of mouse movement on the running wheel and *Z* scored pupil size, overlaid with the binary state of movement (>0.5 cm/s) or pupil dilation (>1 *Z* score).

(B) Bottom: significant ($p < 0.01$) Spearman correlation coefficients (ρ, Rho) of each axon's ΔF/F activity with running speed (cm/s) vs. binary movement state (0 or 1) (left), or *Z* scored pupil size vs. binary dilated state (right). Each dot represents one axon, color-coded by source and target area; only axons with significant correlations to both actual and binary measures are included. Dashed lines: linear-regression fits for each subset, showing relationships between actual and binary movement or pupil size. Top: distribution of absolute deviations from the identity line (|Δ| = Rho _actual – Rho _binary) for each group, summarizing how closely each axon's correlations to actual vs. binary measures align. Positive values indicate stronger correlation with the binary measure, and negative values indicate stronger correlation with the continuous measure. Differences between groups were tested using the Mann-Whitney U test, with *p* values corrected for multiple comparisons using the Benjamini-Hochberg false discovery rate (FDR) method. Movement: ACA-VISp 2,720 axons (4 mice), ORB-VISp 1,289 axons (4 mice), ACA-MOp 4,691 axons (4 mice), ORB-MOp 4,704 axons (4 mice). Pupil: ACA-VISp 2,573 axons (4 mice), ORB-VISp 1,191 axons (4 mice), ACA-MOp 4,299 axons (4 mice), ORB-MOp 4,494 axons (4 mice).

(C) Variance explained (R^2) of behavioral parameters from a linear model (face [SVM *Z* scored], pupil [diameter *Z* scored], pupil binary value [0 or 1 if $z >$ top 20th percentile per session], speed [cm/s], speed binary value [0 or 1 if > 0.5 cm/s]) predicted by the axonal activity of ACA or ORB axons in the VISp (left) or MOp (right) during grating sessions. Differences were tested using the Mann-Whitney U test and Benjamini-Hochberg FDR correction. Significance: *$p < 0.05$, **$p < 0.01$, ***$p < 0.001$. Dots: mean R^2 of all imaging sessions; error bars: SEM; lines: individual sessions. Imaging sessions: $n = 14$ ACA-VISp, 14 ORB-VISp, 16 ACA-MOp, and 25 ORB-MOp.

(D) Strength of correlation to actual vs. binary movement (left) or pupil diameter (right) calculated as a binary preference index (BPI) based on variance explained for the binary vs. actual value per recording session. BPI was plotted for each subset of axons by target area. Each boxplot represents quartiles of values, whiskers show the range of BPI values, and outliers are shown as diamonds. *$p < 0.05$ (one-way ANOVA with Tukey's post hoc test).

(E) Variance explained (R^2) of each behavioral parameter added to a linear model predicting single-axon activity (axon ≥ 1% variance explained). The contribution of each parameter is plotted as its proportional share of total explained variance per axon. Bars: mean proportion; error bars: 95% CI. ACA-VISp: 2,940 axons (22 sessions, 4 mice); ORB-VISp: 1,444 axons (19 sessions, 4 mice); ORB-MOp: 5,015 axons (28 sessions, 4 mice); ACA-MOp: 4,999 axons (21 sessions, 4 mice). Bottom: grouping of VISp vs. MOp (pooled across source areas). Differences were tested using the Mann-Whitney U test and Benjamini-Hochberg FDR correction. Significance: *$p < 0.05$, **$p < 0.01$, ***$p < 0.001$.

See also Figure S4.

whether these relationships differed between VISp and MOp (Figures 4A, 4B, and S4A–S4D). In VISp, both ACA and ORB axons (Spearman's correlation Rho for axons with *p* value < 0.01 to both discrete and binary included) correlated more strongly with binary movement states, whereas in MOp, they correlated better with continuous running speed (Figure 4B, left). For pupil size and facial motion, correlations were stronger with discrete than binary measures in both regions (Figures 4B, right and S4A–S4D).

To quantify how well PFC axonal activity tracked behavioral states, we fit a generalized linear model (GLM) to decode each behavioral state from axonal population activity (see STAR Methods). PFC axon activity accounted for a substantial portion of variance in facial motion, pupil size, and locomotion (both continuous and binary measures). In VISp, activity predicted binary movement state better than continuous speed, whereas pupil size was better predicted as a continuous variable (Figures 4C, 4D, S4E, and S4F).

Please cite this article in press as: Ährlund-Richter et al., Distinct roles of prefrontal subregion feedback to the primary visual cortex across behavioral states, Neuron (2025), https://doi.org/10.1016/j.neuron.2025.10.037

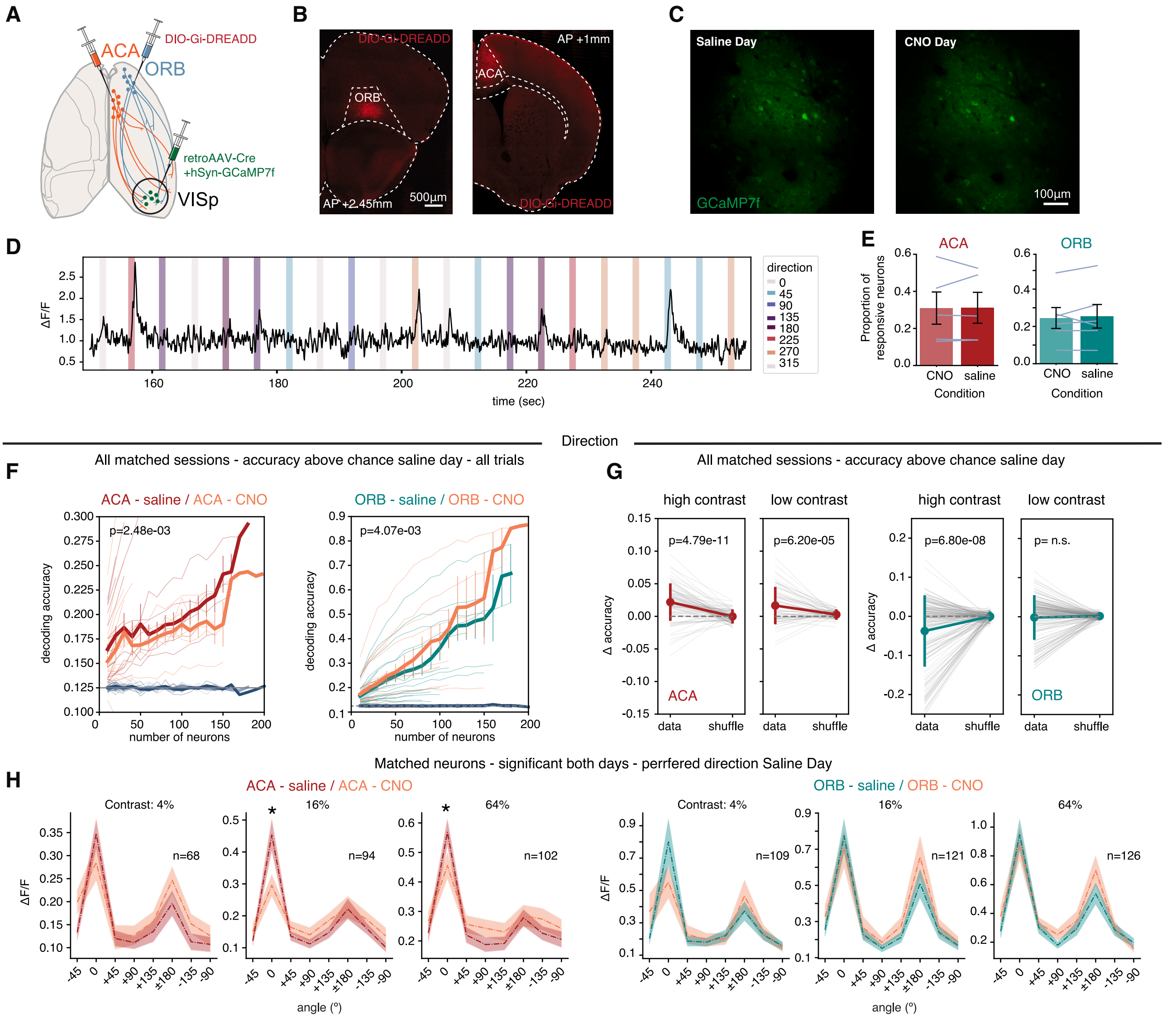

Figure 5. ACA and ORB differentially modulate visual responses of VISp neurons

(A) Experimental strategy. retroAAV-Cre and AAV-hSyn-DIO-GCaMP7f were injected unilaterally into the VISp, followed by Cre-dependent inhibitory designer receptors exclusively activated by designer drugs (DREADDs) (AAV-DIO-hM4D(Gi)-mCherry) into the ACA or ORB. A 3-mm cranial window was implanted above the VISp.

(B) Representative images of viral injection sites in the ACA (left) and ORB (right). Replicated in $n = 5$ ACA and $n = 6$ ORB mice.

(C) Example field of view from 2-photon imaging of GCaMP7f-expressing VISp neurons across two imaging days.

(D) Example activity trace (F) from one VISp neuron, color-coded by drifting grating direction.

(E) Proportion of visually responsive VISp somas in each condition remained stable (Student's paired t test, $p > 0.05$). Bars: mean of proportions; error bars: SEM; lines: individual animals. ACA: saline = 1,760 neurons, CNO = 1,832 neurons ($n = 5$ mice). ORB: saline = 3,228 neurons, CNO = 2,701 neurons ($n = 6$ mice).

(F) Decoding accuracy of an SVM classifier trained and tested on saline-day (red, ACA; green, ORB) or CNO-day (orange) VISp somatic responses (mean ΔF/F during stimuli on-time) per session and field of view. Decoding accuracy of shuffled saline (light gray) and shuffled CNO (dark gray) data plotted for comparison. All paired sessions with accuracy above chance on saline day were included. All trials were included regardless of behavioral state. Thick line: mean accuracy; thin lines: individual sessions; error bars: 95% CI; dashed line: chance level. ACA: 26 paired sessions ($n = 5$ mice); ORB: 33 paired sessions ($n = 6$ mice). Two-way ANCOVA tested effects of subset (neuron number) and condition (saline vs. CNO) on decoding accuracy, including interaction terms to explore if the effect of subset on accuracy varies by group and data/shuffled data. Group effects (saline vs. CNO): ACA, $p = 0.0025$; ORB, $p = 0.0041$.

(G) Decoding accuracy of SVMs trained and tested on VISp somatic responses (mean ΔF/F during stimuli on-time) to high- (64%) or low-contrast (4% and 16%) gratings. Change in decoding accuracy per paired session and neuron subset compared between real and shuffled data. Bars: mean Δ accuracy; error bars: SD; gray lines: paired real and shuffled data from the same session. p values: paired t test. ACA: high-contrast $p = 4.79 \times 10^{-11}$, low-contrast $p = 6.20 \times 10^{-5}$; ORB:

(legend continued on next page)

Please cite this article in press as: Ährlund-Richter et al., Distinct roles of prefrontal subregion feedback to the primary visual cortex across behavioral states, Neuron (2025), https://doi.org/10.1016/j.neuron.2025.10.037

Finally, we used a linear model to predict the activity of PFC axons from visual stimuli and behavioral variables recorded during the imaging sessions (Figures 4E and S4G). Visual stimuli contributed more to predicting PFC axonal activity in VISp than in MOp, but behavioral variables overall explained a larger portion of variance in both regions. In MOp, running speed was the dominant predictor, whereas in VISp, binary speed and pupil size contributed most (Figures 4E and S4G). Hence, differences in parameter contributions were more pronounced across target regions (VISp vs. MOp) than between source areas (ACA vs. ORB).

In summary, our analysis reveals a previously unrecognized functional organization of PFC axonal activity, encompassing both shared and unique activity profiles between PFC subregions and between target regions. This activity is characterized by four distinct traits: (1) ACA axons are responsive to both visual contrast and graded arousal level, (2) ORB axons reflect a more binary arousal-dependent modulation of VISp, (3) ACA and ORB projections to MOp preserve contrast encoding and arousal modulation, but with weaker visual information strength compared with VISp, and (4) PFC axonal activity in both VISp and MOp scales with pupil size, reflecting differential encoding of movement and arousal states, with movement modulation being binary in VISp and continuous in MOp (Figure S9). Thus, while both the ACA and ORB preferentially convey visual information to VISp, ACA conveys more information with respect to both visual contrast and arousal.

ACA and ORB differentially modulate VISp visual responses

The next pivotal question was how the PFC axonal feedback we observed influences the activity of VISp neurons and, importantly, the representation of visual stimuli. Prior studies using optogenetics showed that ACA axons sharpen VISp excitatory neuron tuning via local interneurons.[17] However, it remains unknown how endogenous, behavior-driven PFC activity modulates visual processing, particularly the role of discrete PFC subregions. We injected retroAAV-Cre into VISp and AAV-DIO-hM4D(Gi) into ACA or ORB to enable projection-specific inhibition and later injected AAV-hSyn-GCaMP7f in VISp to image calcium activity in the same experimental conditions as the axonal imaging (Figures 5A, 5B, and 5D). The same VISp neurons were imaged across 2 days in which the mouse received an injection of either saline or CNO (clozapine-N-oxide, 1 mg/kg) (Figure 5C). Recorded neurons identifiable across both days (see STAR Methods) were used to compare single-neuron responses with and without ACA or ORB feedback (dataset referred to as “matched” throughout the paper). The proportion of visually responsive neurons and the behavior of the mice (pupil size, face movement, and running speed) did not differ between conditions (Figures 5E and S5).

To assess how PFC feedback influences visual encoding, we trained an SVM to decode visual stimuli from mean ΔF/F activity of VISp neurons (stratified by contrast and direction) in each session. Paired sessions from the same field of view (saline vs. CNO) were analyzed when decoding accuracy exceeded chance in the saline condition. Notably, ACA and ORB silencing had opposite effects: silencing ACA inputs reduced decoding accuracy for grating direction, whereas silencing ORB inputs paradoxically improved decoding (Figure 5F). While averaged decoding accuracy was higher overall in the ORB group compared with the ACA group (Figure 5F), this likely reflects between-session variability, as the direction and significance of modulation effects were consistent across paired sessions and stimuli (Figures 5G and S6). Given that ACA, but not ORB, axonal activity scaled with contrast in VISp, the effect of contrast on the decoding accuracy was evaluated by training an SVM on trials with either high (64%) or low (4% and 16%) contrast stimuli. Removing ACA input impaired decoding for both high (64%) and low (4% and 16%) contrast gratings (Figure 5G, left), but selectively reduced decoding of low-contrast natural movies (Figures S6C and S6D). By contrast, ORB silencing enhanced decoding for high-contrast gratings and movies only (Figures 5G, right, S6A, and S6B). Analysis of matched individual VISp neurons confirmed that ACA modulation increased response amplitude at the preferred direction across contrasts, whereas ORB removal had no effect (Figure 5H).

To summarize, discrete PFC subregions differentially influence the responses of VISp neurons to visual stimuli. ACA input enhances stimulus encoding and the direction selectivity of matched VISp neurons (Figures 5F and 5H, left), while conversely ORB input appears disruptive to the encoding of high-contrast stimuli (Figure 5F).

ACA modulation of VISp is dependent on arousal state

Behavioral state strongly influences cortical activity, and VISp responses are known to vary with behavioral state (body movement, pupil size, and facial motion).[29,31] Because ACA and ORB axonal activity also correlated with these variables, we next tested whether their modulation of VISp activity depended on behavioral state. As described previously,[29,32] visually responsive VISp neurons showed higher mean and peak ΔF/F responses during arousal or running compared with neutral conditions (Figures 6A and 6B, saline condition). Silencing either ACA or ORB input reduced the arousal-related increase in response amplitude, while only ORB silencing diminished the running-related enhancement (Figures 6A and 6B). These effects were not due to changes in behavior between saline and CNO sessions (Figures 5E and S5). The latency of visual responses was also not affected by ACA or ORB silencing (Figure S7A).

Further investigating the effect of ACA and ORB silencing on matched VISp neurons revealed that the reduction in response

high-contrast $p = 6.80 \times 10^{-8}$, low-contrast $p = 0.37$. High-contrast trials: ACA = 20 sessions ($n = 5$ mice), ORB = 31 sessions ($n = 6$ mice); low-contrast: ACA = 20 sessions ($n = 5$ mice), ORB = 30 sessions ($n = 6$ mice).

(H) Tuning curves of matched VISp neurons responsive on both days to the same direction(s), aligned to preferred direction (determined from saline day), plotted per contrast. All trials were included regardless of behavioral state. Thick line: mean; shaded area: 95% CI. ACA: 4% = 68, 16% = 94, 64% = 102 neurons ($n = 5$ mice); ORB: 4% = 109, 16% = 121, 64% = 126 neurons ($n = 6$ mice). Paired t test ΔF/F responses across matched neurons per direction: ACA 16% $p < 0.0001$, 64% $p < 0.0001$.

See also Figures S5 and S6.

Please cite this article in press as: Ährlund-Richter et al., Distinct roles of prefrontal subregion feedback to the primary visual cortex across behavioral states, Neuron (2025), https://doi.org/10.1016/j.neuron.2025.10.037

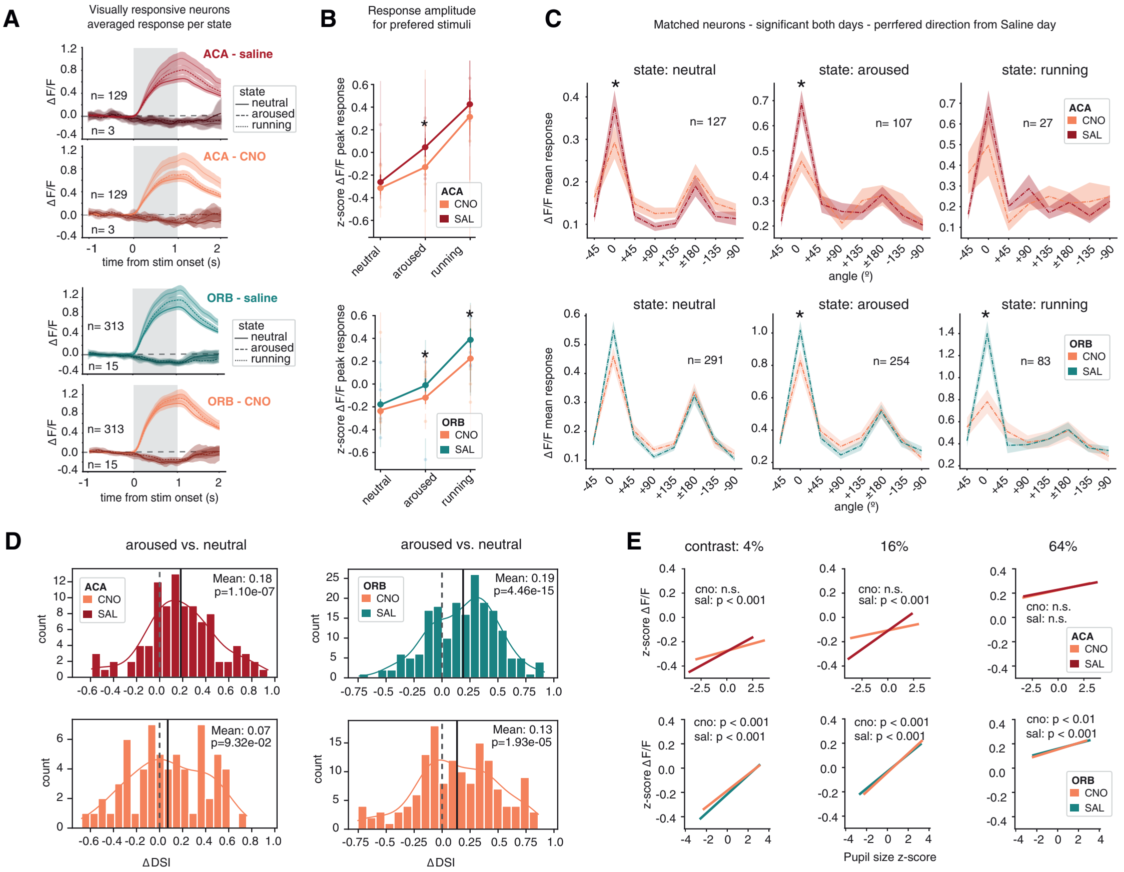

Figure 6. ACA modulation of responses to weak stimuli relates to arousal state

(A) Averaged population responses of matched VISp neurons significantly visually responsive on both days to the same direction(s), plotted per behavioral state and response direction. Behavioral states were defined as the top 20th percentile of trials per session (running speed: movement; pupil size: arousal; <80th percentile: neutral). VISp neurons were classified as positively or negatively tuned based on whether their mean response during stimulus presentation was above or below zero. Top: ACA-DREADDs (132 neurons, 5 mice); bottom: ORB-DREADDs (328 neurons, 6 mice). Thick line: mean; shaded area: 95% CI.

(B) Standardized ΔF/F peak responses during stimulus on-time of matched neurons significantly visually responsive on both days to the same direction(s), plotted per behavioral state (classified as in A). ΔF/F responses were Z scored across each neuron. Bars: mean standardized ΔF/F responses; error bars: 95% CI; dots: individual animals. $^*p < 0.01$ (one-way ANOVA with Tukey's post hoc test for multiple comparisons of means). Top: ACA-DREADDs (132 neurons, 5 mice); bottom: ORB-DREADDs (328 neurons, 6 mice).

(C) Tuning curves of matched neurons significantly visually responsive on both days to the same direction(s), aligned to preferred direction (determined from saline day), plotted per behavioral state. Only neurons with at least one trial per direction in that state were included. Thick line: mean; shaded area: 95% CI. Top: ACA-DREADDs (neutral $p < 0.0001$; aroused $p < 0.0001$); bottom: ORB-DREADDs (aroused $p < 0.0001$; running $p < 0.0001$); paired t test ΔF/F across matched neurons per direction. Top: ACA-DREADDs (neutral 127, arousal 107, running 27 neurons, and 5 mice); bottom: ORB-DREADDs (neutral 291, arousal 254, running 83 neurons, and 6 mice).

(D) Histogram of direction selectivity index (ΔDSI) change from neutral to aroused state (top 20th percentile pupil events). ΔDSI values were calculated for matched neurons significantly visually responsive on both days to the same direction(s), aligned to the preferred direction on saline day. dashed line: 0; solid line: mean ΔDSI. p values from one-sample t test against 0. ACA-DREADDs: saline $p = 1.10 \times 10^{-7}$ (mean = 0.18), CNO $p = 0.093$ (mean = 0.07). ORB-DREADDs: saline $p = 4.46 \times 10^{-15}$ (mean = 0.19), CNO $p = 1.93 \times 10^{-5}$ (mean = 0.13). ACA-DREADDs: saline 97, CNO 64 neurons (5 mice); ORB-DREADDs: saline 146, CNO 191 neurons (6 mice).

(E) Linear regression between Z scored single-trial ΔF/F activity and Z scored pupil size per condition (saline/CNO) and contrast, from matched neurons significantly visually responsive on both days to the same direction(s). ΔF/F mean responses per trial were Z scored across each neuron and condition. Slopes and significance were determined by ordinary least square (OLS) regression. Top: ACA-DREADDs—saline 4%: $p = 4.87 \times 10^{-5}$, slope = 0.05; 16%: $p = 3.72 \times 10^{-8}$, slope = 0.06; 64%: $p = 0.16$, slope = 0.01; CNO 4%: $p = 0.043$, slope = 0.02; 16%: $p = 0.10$, slope = 0.02; 64%: $p = 0.10$, slope = 0.02 (152 neurons, 5 mice; 49,290 total trials—24,737 CNO, 24,553 saline). Bottom: ORB-DREADDs—saline 4%: $p = 4.5 \times 10^{-21}$, slope = 0.07; 16%: $p = 2.61 \times 10^{-27}$, slope = 0.08; 64%: $p = 4.3 \times 10^{-4}$, slope = 0.03; CNO 4%: $p = 6.8 \times 10^{-25}$, slope = 0.08; 16%: $p = 8.3 \times 10^{-22}$, slope = 0.07; 64%: $p = 0.001$, slope = 0.02 (380 neurons; 120,652 total trials—60,336 CNO, 60,316 saline).

See also Figures S7 and S8.

amplitude between saline and CNO sessions reflected decreased responses to the preferred grating direction, rather than a uniform decrease across directions (Figure 6C). In matched neurons aligned to their saline-day preference, ACA silencing reduced response amplitude to the preferred direction in both neutral and aroused states, while responses to other directions were unaffected. ORB silencing decreased preferred-direction responses during aroused and running states but not during neutral conditions (Figure 6C).

Because the effects of PFC silencing were specific to a neuron's preferred direction, we next examined how the direction selectivity index (DSI) of VISp neurons changed across behavioral states with or without ACA or ORB input (Figures 6D and S7A). Neuronal DSI increases from neutral to aroused states, but this effect is abolished when ACA feedback is silenced (Figure 6D, left). By contrast, ORB silencing reduced but did not abolish the increase in DSI from the neutral to aroused state (Figure 6D, right).

Finally, we examined how changes in response amplitude from neutral to aroused depended on stimulus contrast, given the distinct effects of ACA and ORB modulation on contrast encoding (Figure 5G). ACA modulation of low-contrast stimuli was strongly correlated with pupil size, indicating arousal-dependent scaling of response amplitude, a relationship lost when ACA input was silenced (Figure 6E). By contrast, ORB silencing had no effect on this modulation. During transitions from neutral to running states, VISp neurons showed increased DSI values and higher response amplitudes correlated with running speed, and these movement-related effects were unaffected by ACA silencing and only modestly reduced by ORB silencing (Figures S7B and S7C). This scaling of visual responses with running speed likely reflects global neuromodulatory or locomotor influences rather than direct PFC input, as ACA and ORB axonal activity primarily encoded binary movement states in VISp.

We used a GLM to assess how visual and behavioral parameters predicted VISp neuronal activity with or without ACA or ORB silencing. The proportional contribution of each parameter to the explained variance showed no major differences between conditions (Figure S8A). Thus, although ACA and ORB inputs modulate VISp neuronal activity and visual responses, they do not alter the overall encoding of sensory and behavioral information in VISp neurons.

To conclude, our data indicate that ACA feedback strengthens the representation of visual stimuli, particularly low-contrast (low-evidence) stimuli, by increasing the response amplitude of VISp neurons to their preferred direction, resulting in an increase in population decoding accuracy. The modulation of visually responsive VISp neurons by the ACA is dependent on arousal state, and correspondingly, the increase in response amplitude to low-contrast stimuli is largest during high-arousal states. ORB feedback also contributes to the increase in VISp neuron preferred direction responses, especially during running and high-arousal states.

DISCUSSION

In this study, we show that VISp and MOp receive direct projections from two distinct PFC subregions, the ACA and ORB. These projections target both excitatory and inhibitory neurons, indicating complex influence over local microcircuits. By an unbiased analysis in freely observing and locomoting mice, we found that the two projection populations showed distinct differences in their encoding of visual stimuli, whereby ACA axons were more visually responsive and scaled their response with visual contrast unlike ORB axons. Both PFC projections were modulated by behavioral states of locomotion and arousal, putatively through neuromodulatory inputs.[33,34] Comparing PFC feedback between VISp and MOp revealed that feedback to VISp carries a stronger representation of visual information at the population level, while feedback to MOp is more strongly correlated with the animal's speed. Notably, the two PFC regions diverged in their representation of body movement in downstream regions: in VISp, movement was encoded as a binary state, while in MOp axonal activity encoded discrete velocities (Figure S9). These differences between ACA and ORB feedback to VISp and MOp suggest distinct neuronal subpopulations within ACA and ORB, forming discrete functional subnetworks previously described only anatomically.[8] As suggested by the differences in their axonal activity in VISp, silencing ACA or ORB inputs to VISp revealed divergent effects on visual encoding. On a single-cell level, ACA modulation increased VISp neurons' response to their preferred direction. While ORB modulation had no effect on VISp tuning curves in a neutral state, ORB feedback increased neurons' response to their preferred direction during high arousal. Thus, ACA and ORB provide both shared and specialized feedback to VISp and MOp.

ACA and ORB projections innervated distinct VISp layers, with ACA axons targeting layers 1 and 6 and ORB axons targeting layers 1 and 5 (Figures 1D–1F). ACA and ORB have previously been shown to target and activate different VISp interneurons,[7,8,16] a distinction further supported here by our anatomical tracing and functional data. Intriguingly, in this study, cortex-wide mapping revealed that this differential targeting of deep layers extends across the broader "medial" or "visual-medial" network of PFC projections[5,7,8]), whereas in "sensorimotor" or "central" networks, ACA and ORB axons showed similar laminar innervation (Figures S1F and S1H). These findings are complemented by our functional imaging results, in which a difference in laminar organization may underlie the distinct representation and modulation of visual stimuli observed in VISp, while their shared laminar distribution in MOp could account for the similar representation of movement. Together, these findings suggest that ACA and ORB projection populations form discrete functional subnetworks that selectively modulate either visual or motor cortical processing. Future studies should assess whether subgranular feedback arises from separate PFC subpopulations.[9]

The proportion of visually responsive ACA axons observed here (Figures 2F and 2G) matched previous reports for both ACA axons in VISp[30] and ACA cell bodies.[35] ACA axonal responses in both VISp and MOp scaled with stimulus contrast (Figures 2H, 2I, and S2A–S2D). Fewer ORB axons were visually responsive, and their responses showed minimal contrast dependence. This divergence is likely due to differences in whole-brain connectivity. The ACA is known to predominantly share connectivity with the "medial network" of the cortex, including visual cortex regions, RSP, and auditory cortex, in addition to visual thalamic nuclei and areas in the striatum with input from the aforementioned regions.[7,36–38] The ORB, while also having connectivity with the medial network, is more connected to the somatosensory and motor cortical and thalamic regions than the ACA.[7,36–38] Notably, differences in contrast sensitivity and behavioral modulation between ACA and ORB axons were consistent across both VISp and MOp, though overall visual encoding strength varied (Figures 2E and S2). This consistency suggests that visually responsive axons in MOp may represent collaterals from medial-network projections of ACA and ORB.[8]

Changes in locomotion and arousal states strongly shape sensory processing in the mouse cortex, influencing how visual information is represented.[29,39] Visual responses of both ACA and ORB axons were found to also reflect the behavioral state of the animal (Figures 2K and 2L). Likely, state- and movement-related inputs target these PFC regions, as shown for other cortical areas,[33,34] and this is reflected in their feedback. ACA responses and population decoding accuracy scaled with arousal level, measured by pupil size (Figures 2L and 3E). By contrast, ORB axon responses and decoding accuracy increased only during high-arousal periods (Figures 2L and 3F). Therefore, the incorporation of state-dependent modulation into the activity of these discrete projection populations appears distinct. Previous work linked PFC feedback to visual learning and attention,[17,18] and our findings extend this by showing that fluctuations in behavioral state dynamically influence their activity and, consequently, visual encoding in VISp.

The vast majority of ACA and ORB axon activity showed significant correlations with behavioral variables, including face movement, running speed, and pupil size (Figures S4A and S4C). Interestingly, their behavioral tuning differed across target regions: in VISp, ACA, and ORB, axonal activity reflected a binary stationary/moving state, while in MOp, they scaled continuously with running velocity (Figures 4A–4D), indicating that distinct movement-related PFC subpopulations selectively target VISp or MOp. This dichotomy suggests a functional specialization, and PFC feedback to VISp may signal the occurrence of movement independent of velocity, predicting changes in the visual scene, whereas feedback to MOp conveys graded information about movement magnitude, consistent with its role as a central hub of motoric actions. Similar binary movement-related signals have been observed in cholinergic basal forebrain axons projecting to VISp.[40] Importantly, ACA axonal activity in the VISp may predict visual information to appear based on previous experiences in visual space[20] and visual flow due to movement.[19] The activity of ACA and ORB axons we observe could serve a similar function, and our current data provide a baseline for future studies of top-down influences on sensory and motor representations.

While axonal imaging reveals the information conveyed to downstream targets, how does this alter how local circuits process or represent sensory input?[3,4,41] Using two-photon imaging and chemogenetic silencing, we compared how the same VISp neuronal populations encoded visual stimuli with or without ACA or ORB feedback. Silencing ORB input did not alter the tuning curve shape but enhanced decoding accuracy for high-contrast stimuli (Figures 5F–5H and S6). The ORB has been repeatedly associated with reward- and value-related encoding[42–45] and has been directly implicated in modulating VISp responses by outcome expectation.[18] Thus, the reduced decoding accuracy of high-contrast stimuli in the intact condition may reflect ORB-mediated suppression of non-relevant or unrewarded sensory input. Alternatively, ORB feedback linked to movement could interfere with visual cortical processing, akin to movement-related modulation described in the primate visual cortex.[46,47]

Prior work showed that optogenetic activation of the ACA-VISp circuit enhances VISp responses[17]; however, the relationship of optogenetic activation to physiological activity patterns during behavioral states is unclear, and the effect of behavioral state was not examined. Endogenously heightened ACA axonal activity in VISp does not reflect a similar sharpening of VISp neurons' tuning curves.[30] Rather, endogenous ACA axonal activity levels are strongly related to behavioral state.[19,20,30,48] Importantly, our findings unify these prior observations by showing that behavioral state modulates visual encoding by ACA axons in VISp, in particular, the representation of low-contrast stimuli (Figures 2 and 3). Consistent with this, we also observe that ACA feedback increases the response amplitude of VISp neurons toward their preferred stimuli and population-level decoding, particularly at low contrasts, and that this modulation scales with arousal level (Figures 5F–5H, S6, 6D, and 6E). The ACA therefore likely works to enhance the representation of weak or uncertain stimuli during states of arousal and allocated attention. Our findings also reveal a similar dichotomy in ACA and ORB modulation during passive viewing to that observed during visually guided behavior in mice[17,18] as well as a suggested functional dichotomy in the primate.[49]

To conclude, our study reveals that the PFC targets the VISp through two distinct populations of projection neurons originating from the ACA and the ORB. ACA and ORB axons have distinct laminar distributions in VISp, reflecting their potentially complementary roles in the modulation of visual processing. ACA projections are more visually responsive and scale their response to the contrast of visual stimuli, while ORB projections do not exhibit such scaling. Both types of PFC projections are modulated by behavioral states, showing increased response amplitudes during high arousal and movement, albeit with distinct scaling. The distinct representation of visual information and differential encoding of movement in PFC axons within the MOp and the VISp is consistent with a mixture of shared and distinct projection subnetworks within each PFC subregion. The removal of each PFC subregion's input to the VISp results in both unique and shared consequences on the activity of VISp neurons: neuronal activity modulated by high arousal and movement is both decreased, while the encoding of visual information worsens in the absence of ACA input and is surprisingly enhanced in the absence of ORB input (Figure S9). Such a differential impact likely reflects distinct local microcircuitry that is targeted by ACA and ORB inputs to VISp, and unraveling the interplay of these downstream targets is a critical goal for future work.

RESOURCE AVAILABILITY

Lead contact

Requests for further information and resources should be directed to and will be fulfilled by the lead contact, Mriganka Sur (msur@mit.edu).

Materials availability

This study did not generate new, unique reagents.

Data and code availability

- All data reported in this paper will be shared by the lead contact upon reasonable request.
- This paper does not report original code.
- Any additional information required to reanalyze the data reported in this paper is also available from the lead contact upon request.

ACKNOWLEDGMENTS

This research was supported by the Wenner-Gren Foundation's Postdoctoral Fellowship WGF2020-0019, NIH grant K99EY035752 (to S.Ä.-R.), NIH grant F32EY032756 (to K.R.J.), NIH grant R01MH139680 (to D.B.A.), NIH grants R01MH133066 and R01NS130361, and the Picower Institute Innovation Fund (to M.S.). We thank Yi Ning Leow and Greggory Heller for thoughtful discussions, Alexandria Barlowe and Jonathan Harpe for assistance with histology, Taylor Johns for administrative and technical assistance, Marco Celotto for aiding with the decoding analysis, and Cantin Ortiz for aiding with the creation of the axon tracing pipeline.

AUTHOR CONTRIBUTIONS

S.Ä.-R. conceived the study, designed and performed the experiments, analyzed the data, and wrote the manuscript. Y.O. designed the SVM decoder and GLM. K.R.J. built the behavioral rig, aided with experimental design and analysis, and provided extensive input to the manuscript. E.O. performed the immunohistological analysis of the ATLAS virus tracing. H.H. and D.B.A. provided the unpublished ATLAS virus system and aided with its use. M.S. contributed to the direction of data analysis and the development of presented concepts, enabled execution of the study, and contributed to the writing of the manuscript. All authors provided input to the manuscript.

DECLARATION OF INTERESTS

The authors declare no competing interests.

DECLARATION OF GENERATIVE AI AND AI-ASSISTED TECHNOLOGIES IN THE WRITING PROCESS

During the preparation of this work, the author(s) used OpenAI/ChatGPT in order to improve the readability of the manuscript. After using this tool/service, the author(s) reviewed and edited the content as needed and take(s) full responsibility for the content of the publication.

STAR★METHODS

Detailed methods are provided in the online version of this paper and include the following:

- KEY RESOURCES TABLE
- EXPERIMENTAL MODEL AND STUDY PARTICIPANT DETAILS
    - ○ Animal subjects
- METHOD DETAILS
    - ○ Viral injections and implants
    - ○ Anatomical and Histological analysis
    - ○ Behavioral setup
    - ○ Two-photon imaging parameters
    - ○ Preprocessing of behavioral and imaging data
    - ○ DREADD manipulations
- QUANTIFICATION AND STATISTICAL ANALYSIS
    - ○ Analysis
    - ○ Statistical Methods

SUPPLEMENTAL INFORMATION

Supplemental information can be found online at https://doi.org/10.1016/j.neuron.2025.10.037.

Received: February 26, 2025
Revised: September 4, 2025
Accepted: October 30, 2025

REFERENCES

1. Rockland, K.S., and Pandya, D.N. (1979). Laminar origins and terminations of cortical connections of the occipital lobe in the rhesus monkey. Brain Res. *179*, 3–20. https://doi.org/10.1016/0006-8993(79)90485-2.
2. Felleman, D.J., and Van Essen, D.C. (1991). Distributed hierarchical processing in the primate cerebral cortex. Cereb. Cortex *1*, 1–47. https://doi.org/10.1093/cercor/1.1.1-a.
3. Miller, E.K. (2000). The prefrontal cortex and cognitive control. Nat. Rev. Neurosci. *1*, 59–65. https://doi.org/10.1038/35036228.
4. Miller, E.K., and Cohen, J.D. (2001). AN INTEGRATIVE THEORY OF PREFRONTAL CORTEX FUNCTION. Annu. Rev. Neurosci. *24*, 167–202. https://doi.org/10.1146/annurev.neuro.24.1.167.
5. Harris, J.A., Mihalas, S., Hirokawa, K.E., Whitesell, J.D., Choi, H., Bernard, A., Bohn, P., Caldejon, S., Casal, L., Cho, A., et al. (2019). Hierarchical organization of cortical and thalamic connectivity. Nature *575*, 195–202. https://doi.org/10.1038/s41586-019-1716-z.
6. Le Merre, P.L., Ährlund-Richter, S., and Carlén, M. (2021). The mouse prefrontal cortex: Unity in diversity. Neuron *109*, 1925–1944. https://doi.org/10.1016/j.neuron.2021.03.035.
7. Zingg, B., Hintiryan, H., Gou, L., Song, M.Y., Bay, M., Bienkowski, M.S., Foster, N.N., Yamashita, S., Bowman, I., Toga, A.W., et al. (2014). Neural networks of the mouse neocortex. Cell *156*, 1096–1111. https://doi.org/10.1016/j.cell.2014.02.023.
8. Gao, L., Liu, S., Gou, L., Hu, Y., Liu, Y., Deng, L., Ma, D., Wang, H., Yang, Q., Chen, Z., et al. (2022). Single-neuron projectome of mouse prefrontal cortex. Nat. Neurosci. *25*, 515–529. https://doi.org/10.1038/s41593-022-01041-5.
9. Liu, S., Gao, L., Chen, J., and Yan, J. (2024). Single-neuron analysis of axon arbors reveals distinct presynaptic organizations between feedforward and feedback projections. Cell Rep. *43*, 113590. https://doi.org/10.1016/j.celrep.2023.113590.
10. Allen, W.E., Kauvar, I.V., Chen, M.Z., Richman, E.B., Yang, S.J., Chan, K., Gradinaru, V., Deverman, B.E., Luo, L., and Deisseroth, K. (2017). Global Representations of Goal-Directed Behavior in Distinct Cell Types of Mouse Neocortex. Neuron *94*, 891–907.e6. https://doi.org/10.1016/j.neuron.2017.04.017.
11. Makino, H., Ren, C., Liu, H., Kim, A.N., Kondapaneni, N., Liu, X., Kuzum, D., and Komiyama, T. (2017). Transformation of Cortex-wide Emergent Properties during Motor Learning. Neuron *94*, 880–890.e8. https://doi.org/10.1016/j.neuron.2017.04.015.
12. Kamigaki, T. (2019). Prefrontal circuit organization for executive control. Neurosci. Res. *140*, 23–36. https://doi.org/10.1016/j.neures.2018.08.017.
13. Moore, T., and Zirnsak, M. (2017). Neural Mechanisms of Selective Visual Attention. Annu. Rev. Psychol. *68*, 47–72. https://doi.org/10.1146/annurev-psych-122414-033400.
14. Zhang, S., Xu, M., Chang, W.-C., Ma, C., Hoang Do, J.P., Jeong, D., Lei, T., Fan, J.L., and Dan, Y. (2016). Organization of long-range inputs and outputs of frontal cortex for top-down control. Nat. Neurosci. *19*, 1733–1742. https://doi.org/10.1038/nn.4417.
15. Ma, G., Liu, Y., Wang, L., Xiao, Z., Song, K., Wang, Y., Peng, W., Liu, X., Wang, Z., Jin, S., et al. (2021). Hierarchy in sensory processing reflected by innervation balance on cortical interneurons. Sci. Adv. *7*, eabf5676. https://doi.org/10.1126/sciadv.abf5676.

16. Liu, Y., Zhang, J., Jiang, Z., Qin, M., Xu, M., Zhang, S., and Ma, G. (2024). Organization of corticocortical and thalamocortical top-down inputs in the primary visual cortex. Nat. Commun. *15*, 4495. https://doi.org/10.1038/s41467-024-48924-8.

17. Zhang, S., Xu, M., Kamigaki, T., Hoang Do, J.P.H., Chang, W.-C., Jenvay, S., Miyamichi, K., Luo, L., and Dan, Y. (2014). Selective attention. Long-range and local circuits for top-down modulation of visual cortex processing. Science *345*, 660–665. https://doi.org/10.1126/science.1254126.

18. Liu, D., Deng, J., Zhang, Z., Zhang, Z.-Y., Sun, Y.-G., Yang, T., and Yao, H. (2020). Orbitofrontal control of visual cortex gain promotes visual associative learning. Nat. Commun. *11*, 2784. https://doi.org/10.1038/s41467-020-16609-7.

19. Leinweber, M., Ward, D.R., Sobczak, J.M., Attinger, A., and Keller, G.B. (2017). A Sensorimotor Circuit in Mouse Cortex for Visual Flow Predictions. Neuron *95*, 1420–1432.e5. https://doi.org/10.1016/j.neuron.2017.08.036.

20. Fiser, A., Mahringer, D., Oyibo, H.K., Petersen, A.V., Leinweber, M., and Keller, G.B. (2016). Experience-dependent spatial expectations in mouse visual cortex. Nat. Neurosci. *19*, 1658–1664. https://doi.org/10.1038/nn.4385.

21. Oh, S.W., Harris, J.A., Ng, L., Winslow, B., Cain, N., Mihalas, S., Wang, Q., Lau, C., Kuan, L., Henry, A.M., et al. (2014). A mesoscale connectome of the mouse brain. Nature *508*, 207–214. https://doi.org/10.1038/nature13186.

22. Lein, E.S., Hawrylycz, M.J., Ao, N., Ayres, M., Bensinger, A., Bernard, A., Boe, A.F., Boguski, M.S., Brockway, K.S., Byrnes, E.J., et al. (2007). Genome-wide atlas of gene expression in the adult mouse brain. Nature *445*, 168–176. https://doi.org/10.1038/nature05453.

23. Fürth, D., Vaissière, T., Tzortzi, O., Xuan, Y., Märtin, A., Lazaridis, I., Spigolon, G., Fisone, G., Tomer, R., Deisseroth, K., et al. (2018). An interactive framework for whole-brain maps at cellular resolution. Nat. Neurosci. *21*, 139–149. https://doi.org/10.1038/s41593-017-0027-7.

24. Rivera, J.F., Huang, H., Weng, W., Sohn, H., Girasole, A.E., Li, S., Albanese, M.A., Qin, M., Tao, C., Klug, M.E., et al. (2025). ATLAS: a rationally designed anterograde transsynaptic tracer. Nat. Methods *22*, 1101–1111. https://doi.org/10.1038/s41592-025-02670-x.

25. Larkum, M. (2013). A cellular mechanism for cortical associations: an organizing principle for the cerebral cortex. Trends Neurosci. *36*, 141–151. https://doi.org/10.1016/j.tins.2012.11.006.

26. Pachitariu, M., Stringer, C., Dipoppa, M., Schröder, S., Rossi, L.F., Dalgleish, H., Carandini, M., and Harris, K.D. (2017). Suite2p: beyond 10,000 neurons with standard two-photon microscopy. Preprint at bioRxiv. https://doi.org/10.1101/061507.

27. Zhuang, J., Larsen, R.S., Takasaki, K.T., Ouellette, N.D., Daigle, T.L., Tasic, B., Waters, J., Zeng, H., and Reid, R.C. (2020). The spatial structure of feedforward information in mouse primary visual cortex. Preprint at bioRxiv. https://doi.org/10.1101/2019.12.24.888156.

28. Niell, C.M., and Stryker, M.P. (2008). Highly Selective Receptive Fields in Mouse Visual Cortex. J. Neurosci. *28*, 7520–7536. https://doi.org/10.1523/JNEUROSCI.0623-08.2008.

29. Vinck, M., Batista-Brito, R., Knoblich, U., and Cardin, J.A. (2015). Arousal and locomotion make distinct contributions to cortical activity patterns and visual encoding. Neuron *86*, 740–754. https://doi.org/10.1016/j.neuron.2015.03.028.

30. Broom, E., Imbriotis, V., Sengpiel, F., Connelly, W.M., and Ranson, A. (2022). Recruitment of frontal sensory circuits during visual discrimination. Cell Rep. *39*, 110932. https://doi.org/10.1016/j.celrep.2022.110932.

31. Stringer, C., Pachitariu, M., Steinmetz, N., Reddy, C.B., Carandini, M., and Harris, K.D. (2019). Spontaneous behaviors drive multidimensional, brainwide activity. Science *364*, 255. https://doi.org/10.1126/science.aav7893.

32. Reimer, J., Froudarakis, E., Cadwell, C.R., Yatsenko, D., Denfield, G.H., and Tolias, A.S. (2014). Pupil fluctuations track fast switching of cortical states during quiet wakefulness. Neuron *84*, 355–362. https://doi.org/10.1016/j.neuron.2014.09.033.

33. Plummer, N.W., Chandler, D.J., Powell, J.M., Scappini, E.L., Waterhouse, B.D., and Jensen, P. (2020). An Intersectional Viral-Genetic Method for Fluorescent Tracing of Axon Collaterals Reveals Details of Noradrenergic Locus Coeruleus Structure. eNeuro *7*. ENEURO.0010-20.2020. https://doi.org/10.1523/ENEURO.0010-20.2020.

34. Li, X., Yu, B., Sun, Q., Zhang, Y., Ren, M., Zhang, X., Li, A., Yuan, J., Madisen, L., Luo, Q., et al. (2018). Generation of a whole-brain atlas for the cholinergic system and mesoscopic projectome analysis of basal forebrain cholinergic neurons. Proc. Natl. Acad. Sci. USA *115*, 415–420. https://doi.org/10.1073/pnas.1703601115.

35. Kim, J.-H., Ma, D.-H., Jung, E., Choi, I., and Lee, S.-H. (2021). Gated feedforward inhibition in the frontal cortex releases goal-directed action. Nat. Neurosci. *24*, 1452–1464. https://doi.org/10.1038/s41593-021-00910-9.

36. Hunnicutt, B.J., Long, B.R., Kusefoglu, D., Gertz, K.J., Zhong, H., and Mao, T. (2014). A comprehensive thalamocortical projection map at the mesoscopic level. Nat. Neurosci. *17*, 1276–1285. https://doi.org/10.1038/nn.3780.

37. Hintiryan, H., Foster, N.N., Bowman, I., Bay, M., Song, M.Y., Gou, L., Yamashita, S., Bienkowski, M.S., Zingg, B., Zhu, M., et al. (2016). The mouse cortico-striatal projectome. Nat. Neurosci. *19*, 1100–1114. https://doi.org/10.1038/nn.4332.

38. Hunnicutt, B.J., Jongbloets, B.C., Birdsong, W.T., Gertz, K.J., Zhong, H., and Mao, T. (2016). A comprehensive excitatory input map of the striatum reveals novel functional organization. eLife *5*, e19103. https://doi.org/10.7554/eLife.19103.

39. Ferguson, K.A., and Cardin, J.A. (2020). Mechanisms underlying gain modulation in the cortex. Nat. Rev. Neurosci. *21*, 80–92. https://doi.org/10.1038/s41583-019-0253-y.

40. Yogesh, B., and Keller, G.B. (2024). Cholinergic input to mouse visual cortex signals a movement state and acutely enhances layer 5 responsiveness. eLife *12*, RP89986. https://doi.org/10.7554/eLife.89986.

41. Buschman, T.J., and Miller, E.K. (2014). Goal-direction and top-down control. Philos. Trans. R. Soc. Lond. B Biol. Sci. *369*, 20130471. https://doi.org/10.1098/rstb.2013.0471.

42. Kepecs, A., Uchida, N., Zariwala, H.A., and Mainen, Z.F. (2008). Neural correlates, computation and behavioural impact of decision confidence. Nature *455*, 227–231. https://doi.org/10.1038/nature07200.

43. Wang, P.Y., Boboila, C., Chin, M., Higashi-Howard, A., Shamash, P., Wu, Z., Stein, N.P., Abbott, L.F., and Axel, R. (2020). Transient and Persistent Representations of Odor Value in Prefrontal Cortex. Neuron *108*, 209–224.e6. https://doi.org/10.1016/j.neuron.2020.07.033.

44. Jennings, J.H., Kim, C.K., Marshel, J.H., Raffiee, M., Ye, L., Quirin, S., Pak, S., Ramakrishnan, C., and Deisseroth, K. (2019). Interacting neural ensembles in orbitofrontal cortex for social and feeding behaviour. Nature *565*, 645–649. https://doi.org/10.1038/s41586-018-0866-8.

45. Zhou, J., Jia, C., Feng, Q., Bao, J., and Luo, M. (2015). Prospective Coding of Dorsal Raphe Reward Signals by the Orbitofrontal Cortex. J. Neurosci. *35*, 2717–2730. https://doi.org/10.1523/JNEUROSCI.4017-14.2015.

46. Sommer, M.A., and Wurtz, R.H. (2008). Brain Circuits for the Internal Monitoring of Movements. Annu. Rev. Neurosci. *31*, 317–338. https://doi.org/10.1146/annurev.neuro.31.060407.125627.

47. Thiele, A., Henning, P., Kubischik, M., and Hoffmann, K.P. (2002). Neural Mechanisms of Saccadic Suppression. Science *295*, 2460–2462. https://doi.org/10.1126/science.1068788.

48. Chintalacheruvu, N., Kalelkar, A., Boutin, J., Breton-Provencher, V., and Huda, R. (2024). A cortical locus for modulation of arousal states. Preprint at bioRxiv. https://doi.org/10.1101/2024.05.24.595859.

49. Barbas, H. (2022). Frontal Cortex. In Neuroscience in the 21st Century: From Basic to Clinical, D.W. Pfaff, N.D. Volkow, and J.L. Rubenstein, eds. (Springer International Publishing), pp. 1707–1753. https://doi.org/10.1007/978-3-030-88832-9_45.

Please cite this article in press as: Ährlund-Richter et al., Distinct roles of prefrontal subregion feedback to the primary visual cortex across behavioral states, Neuron (2025), https://doi.org/10.1016/j.neuron.2025.10.037

50. Broussard, G.J., Liang, Y., Fridman, M., Unger, E.K., Meng, G., Xiao, X., Ji, N., Petreanu, L., and Tian, L. (2018). In vivo measurement of afferent activity with axon-specific calcium imaging. Nat. Neurosci. *21*, 1272–1280. https://doi.org/10.1038/s41593-018-0211-4.

51. Fenno, L.E., Mattis, J., Ramakrishnan, C., Hyun, M., Lee, S.Y., He, M., Tucciarone, J., Selimbeyoglu, A., Berndt, A., Grosenick, L., et al. (2014). Targeting cells with single vectors using multiple-feature Boolean logic. Nat. Methods *11*, 763–772. https://doi.org/10.1038/nmeth.2996.

52. Krashes, M.J., Koda, S., Ye, C., Rogan, S.C., Adams, A.C., Cusher, D.S., Maratos-Flier, E., Roth, B.L., and Lowell, B.B. (2011). Rapid, reversible activation of AgRP neurons drives feeding behavior in mice. J. Clin. Investig. *121*, 1424–1428. https://doi.org/10.1172/JCI46229.

53. Dana, H., Sun, Y., Mohar, B., Hulse, B.K., Kerlin, A.M., Hasseman, J.P., Tsegaye, G., Tsang, A., Wong, A., Patel, R., et al. (2019). High-performance calcium sensors for imaging activity in neuronal populations and microcompartments. Nat. Methods *16*, 649–657. https://doi.org/10.1038/s41592-019-0435-6.

54. Sciolino, N.R., Hsiang, M., Mazzone, C.M., Wilson, L.R., Plummer, N.W., Amin, J., Smith, K.G., McGee, C.A., Fry, S.A., Yang, C.X., et al. (2022). Natural locus coeruleus dynamics during feeding. Sci. Adv. *8*, eabn9134. https://doi.org/10.1126/sciadv.abn9134.

55. Schindelin, J., Arganda-Carreras, I., Frise, E., Kaynig, V., Longair, M., Pietzsch, T., Preibisch, S., Rueden, C., Saalfeld, S., Schmid, B., et al. (2012). Fiji: an open-source platform for biological-image analysis. Nat. Methods *9*, 676–682. https://doi.org/10.1038/nmeth.2019.

56. Brainard, D.H. (1997). The Psychophysics Toolbox. Spat. Vis. *10*, 433–436. https://doi.org/10.1163/156856897X00357.

57. Mathis, A., Mamidanna, P., Cury, K.M., Abe, T., Murthy, V.N., Mathis, M.W., and Bethge, M. (2018). DeepLabCut: markerless pose estimation of user-defined body parts with deep learning. Nat. Neurosci. *21*, 1281–1289. https://doi.org/10.1038/s41593-018-0209-y.

58. Syeda, A., Zhong, L., Tung, R., Long, W., Pachitariu, M., and Stringer, C. (2023). Facemap: a framework for modeling neural activity based on orofacial tracking. Nat. Neurosci. *27*, 187–195. https://doi.org/10.1038/s41593-023-01490-6.

Please cite this article in press as: Ährlund-Richter et al., Distinct roles of prefrontal subregion feedback to the primary visual cortex across behavioral states, Neuron (2025), https://doi.org/10.1016/j.neuron.2025.10.037

STAR★METHODS

KEY RESOURCES TABLE

REAGENT or RESOURCE	SOURCE	IDENTIFIER
Antibodies		
anti-RFP: rabbit	Rockland	Cat# 600-401-379; RRID:AB_2209751
anti-GFP: chicken	Aves	Cat# GFP-1020; RRID:AB_10000240
anti-PV: guinea pig	ImmunoStar	Cat# 24428; RRID:AB_572259
anti-SST: rat	Millipore Sigma	Cat# MAB354; RRID:AB_2255365
anti-VIP: rabbit	ImmunoStar	Cat# 20077; RRID:AB_572270
anti-Guinea Pig DyLight 405: Donkey	Jackson ImmunoResearch	Cat# 706-475-148; RRID:AB_2340470
anti-Rat Alexa Fluor 647: Donkey	Jackson ImmunoResearch	Cat# 712-605-153; RRID:AB_2340694
anti-Rabbit Alexa Fluor 488: Donkey	Jackson ImmunoResearch	Cat# 711-545-152; RRID:AB_2313584
anti-Chicken Alexa Fluor 488: Donkey	Jackson ImmunoResearch	Cat# 703-545-155; RRID:AB_2340375
anti-Rabbit Alexa Fluor 594: Donkey	Jackson ImmunoResearch	Cat# 711-585-152; RRID:AB_2340621
Experimental models: Organisms/strains		
Mouse: C57BL/6J	Jackson Laboratory	RRID:IMSR_JAX:000664
Mouse: VIP-Flp: $Vip^{tm2.1(flpo)Zjh}$/J	Jackson Laboratory	RRID:IMSR_JAX:028578
Recombinant DNA		
retroAAV-hSyn-GFP	gift from Bryan Roth	Addgene cat# 50465-AAVrg
AAV1-CAG-tdTomato	gift from Edward Boyden	Addgene cat# 59462-AAV1
AAV5-CAG-GFP	gift from Edward Boyden	Addgene cat# 37825-AAV5
AAV8-hsyn-SytNB-ALFAtag-BACEcs-myc-Cre	Center for Neural Circuit Mapping, University of California, Irvine	N/A
AAV.PHP.eB-CAG-DIO-tdTomato	gift from Edward Boyden	Addgene cat# 28306-PHPeB
AAV1-hSyn-axon-GCamP6s	Broussard et al.[50]	Addgene cat# 111262-AAV1
retroAAV-Ef1a-Cre	Fenno et al.[51]	Addgene cat# 55636-AAVrg
AAV-hSyn-DIO-hM4D(Gi)-mCherry	Krashes et al.[52]	Addgene cat# 44362-AAV5
AAV-hSyn-GCamP7f	Dana et al.[53]	Addgene cat# 104488-AAV9
AAV1-Ef1a-fDIO-tdTomato	Sciolino et al.[54]	Addgene cat# 128434-AAV1
Software and algorithms		
WholeBrainSuite R package	Furth et al.[23]	https://github.com/tractatus/wholebrain
Fiji / ImageJ	Schindelin et al.[55]	https://imagej.net/software/fiji/
Psychtoolbox	Brainard[56]	http://psychtoolbox.org/
MATLAB	MathWorks	https://www.mathworks.com/
DeepLabCut	Mathis et al.[57]	https://github.com/DeepLabCut/
FaceMap	Syeda et al.[58]	https://github.com/MouseLand/facemap
Suite2p	Pachitariu et al.[26]	https://github.com/MouseLand/suite2p
ROIMatchPub	N/A	https://github.com/ransona/ROIMatchPub
Python version 3.8.8	Python Software Foundation	https://www.python.org/

EXPERIMENTAL MODEL AND STUDY PARTICIPANT DETAILS

Animal subjects

All experiments were carried out in adult male and female mice under protocols conforming to NIH guidelines approved by the MIT Animal Care and Use Committee. Wild type C57BL/6J, Jackson stock no. 000664, or transgenic mouse line VIP-Flp: $Vip^{tm2.1(flpo)Zjh}$/J, Jackson stock no. 028578 were used. Mice were 2-4 months at the time of surgery and group-housed before and after surgery (max 2 per cage if the mice had head implants for 2-photon imaging). All transgenic mice used in experiments were heterozygous for the transgenes. Mice were maintained under standard housing conditions with a 12-hour light cycle and with *ad libitum* access to food and water.

Please cite this article in press as: Ährlund-Richter et al., Distinct roles of prefrontal subregion feedback to the primary visual cortex across behavioral states, Neuron (2025), https://doi.org/10.1016/j.neuron.2025.10.037

METHOD DETAILS

Viral injections and implants

General procedure

Mice were anesthetized with isoflurane (1.5%) and given preemptive analgesia (extended release buprenex, 1mg/kg, and meloxicam, 5mg/kg, s.c.). After hair removal and sterilization of the skin with 70% ethanol and betadine, the mouse was placed into a stereotaxic frame (51725D, Stoelting). The temperature of the mice was maintained at 36°C with a feedback-controlled heating pad (ATC2000, World Precision Instruments). For viral injections, a micropipette attached on a Quintessential Stereotaxic Injector (QSI 53311, Stoelting) was used (see axonal tracing, axonal imaging, and somatic imaging with DREADDs for details). The pipette was held in place for 5 min after each viral injection before being slowly retracted from the brain. Postoperative analgesics (meloxicam 5mg/kg, s.c.) were given 18-24h after the surgery, and recovery was monitored for a minimum of 72 h after surgery.

Retrograde tracing

A small craniotomy was drilled above the right Primary Visual Cortex (AP: -3.5, ML: -2.5, DV: -0.3) and 0.2μl of retroAAV-hSyn-GFP (50465-AAVrg, Addgene, 7×10^{12} vg/mL) was injected at a rate of 0.05μl/min. Retrograde transport and virus expression was allowed for 2 weeks before the mouse was perfused for tissue collection.

Axonal tracing

A small craniotomy was drilled above the right Anterior Cingulate Cortex (AP: +1, ML: -0.3, DV: -0.9) and 0.2μl of AAV1-CAG-tdTomato (59462-AAV1, Addgene, 5×10^{12} vg/mL) was injected at a rate of 0.05μl/min. A second craniotomy was drilled above the Orbitofrontal Cortex (AP: +2.45, ML: -1.1, DV: -1.75) and 0.2μl of AAV5-CAG-GFP (37825-AAV5, Addgene, 7×10^{12} vg/mL) was injected at a rate of 0.05μl/min. Virus expression was allowed for 4 weeks before the mouse was perfused for tissue collection.

Anterograde tracing

A small craniotomy was drilled above the right Anterior Cingulate Cortex (AP: +1, ML: -0.3, DV: -0.9) or Orbitofrontal Cortex (AP: +2.45, ML: -1.1, DV: -1.75) and 0.3μl of AAV8-hsyn-SytNB-ALFAtag-BACEcs-myc-Cre (Center for Neural Circuit Mapping, University of California, Irvine, 1×10^{13} gc/mL) was injected at a rate of 0.05μl/min. A second craniotomy was performed over the Visual (AP: -3.5, ML: -2.5, DV: -0.4) and the Motor Cortex (AP: +0.5, ML: -1.5, DV: -0.4) and 0.3μl of AAV.PHP.eB-CAG-DIO-tdTomato (28306-PHPeB, Addgene, $1\times10^{1}3$ vg/mL) was injected at a rate of 0.05μl/min. Virus expression was allowed for 4 weeks before the mouse was perfused for tissue collection.

Axonal Imaging

A small craniotomy was drilled above the Anterior Cingulate Cortex (AP: +1, ML: -0.3, DV: -0.9) or Orbitofrontal Cortex (AP: +2.45, ML: -1.1, DV: -1.75) and 0.2μl of AAV1-hSyn-axon-GCamP6s (111262-AAV1, Addgene, 7×10^{12} vg/mL) was injected at a rate of 0.05μl/min. A round 3mm craniotomy was performed over the Visual (AP: -3.5, ML: -2.5) or Motor Cortex (AP: +0.5, ML: -1.5). A cranial window made of three round coverslips (CS-5R, 1x5 mm diameter; CS-3R, 2x3 mm diameter; Warner Instruments) glued together with UV-cured adhesive (catalog #NOA 61, Norland) was implanted over the craniotomy and sealed with dental cement (C&B Metabond, Parkell). For head fixation during the calcium imaging, a head plate was also affixed to the skull using dental cement (C&B Metabond, Parkell).

Somatic imaging with DREADDs

A small craniotomy was drilled above the Visual Cortex (AP: -3.5, ML: -2.5, DV: -0.3) and two adjacent injections of 0.2μl retroAAV-Ef1a-Cre (55636-AAVrg, Addgene, 7×10^{12} vg/mL) were injected at a rate of 0.05μl/min. After the retraction of the injection needle the craniotomy was filled with bone wax (Medline). A small craniotomy was then drilled above the Anterior Cingulate Cortex (AP: +1, ML: -0.3, DV: -0.9) or ORB (AP: +2.45, ML: -1.1, DV: -1.75) and 0.2μl AAV-hSyn-DIO-hM4D(Gi)-mCherry (44362-AAV5, Addgene, 7×10^{12} vg/mL) was injected at a rate of 0.05μl/min. The skin incision on top of the skull was then closed with sutures. Two weeks after the first surgery, a second larger (3mm) craniotomy was made over the Visual Cortex, and four small injections of a mixture of 1:20 AAV-hSyn-GCamP7f (104488-AAV9, Addgene, 1×10^{13} vg/mL) and 1:5 AAV1-Ef1a-fDIO-tdTomato (128434-AAV1, Addgene, 1×10^{13} vg/mL) was made into the craniotomy. Thereafter, a cranial window made of three round coverslips (CS-5R, 1x5 mm diameter; CS-3R, 2x3 mm diameter; Warner Instruments) glued together with UV-cured adhesive (catalog #NOA 61, Norland) was implanted over the craniotomy and sealed with dental cement (C&B Metabond, Parkell). For head fixation during the calcium imaging, a head plate was also affixed to the skull using dental cement (C&B Metabond, Parkell).

Anatomical and Histological analysis

General procedure

Following an overdose of isoflurane, all mice were transcardially perfused with 1x PBS followed by 4% paraformaldehyde in PBS. Brains were left over night in 4% PFA and washed three times in PBS the following day.

Axonal tracing

The whole brain was cut coronally at a thickness of 50μm using a vibratome (VT1200S, Leica). Every other section was thereafter collected. The collected sections were placed free-floating in 1× PBST (0.3% Triton-X in 1× PBS) for 1 h, and subsequently incubated with primary antibodies at a concentration of 1:1000 in PBST (anti-RFP: rabbit, 600-401-379, Rockland and anti-GFP: chicken, GFP-1020, Aves) overnight in room temperature. The following day the sections were washed three times in PBST and incubated with secondary antibodies (anti-Chicken Alexa Fluor 488: Donkey, 703-545-155, Jackson ImmunoResearch and anti-Rabbit Alexa Fluor

Please cite this article in press as: Ährlund-Richter et al., Distinct roles of prefrontal subregion feedback to the primary visual cortex across behavioral states, Neuron (2025), https://doi.org/10.1016/j.neuron.2025.10.037

594: Donkey, 711-585-152, Jackson ImmunoResearch) at a concentration of 1:1000 in PBST for 3-5h in room temperature. The sections were consecutively washed with 1× PBST, 1× PBS and 1× PBS (10 min each). Vibratome cut sections were mounted on glass slides (Superfrost Plus, Thermo Scientific). All sections were coverslipped (Thermo Scientific) using 50:50 glycerol:1× PBS. Tiled whole-brain images were acquired of both the green and red channel using a Leica TCS SP8 confocal microscope using a 10X / 0.40 NA objective.

For the whole-brain axonal mapping of the two projections, the axonal labeling (each fluorescent pixel) was segmented out using a custom macro in ImageJ and the coordinates of each axon-labeled pixel was saved. Each section was thereafter manually assigned an AP coordinate and mapped to the Allen Brain Atlas (2011 version[22]) using a custom R-script utilizing the WholeBrainSuite R package.[23] The segmented axons were then mapped back onto the section and a pixel density value (axon-labeled pixels / total pixels) and axon density ($\mu m^2_{axon}/\mu m^2_{total\ area}$) for each brain region and layer were produced for each brain section. To avoid an overrepresentation of axonal density at each injection site, the segmentation method was modified to only extract pixels representing cell bodies without the surrounding neuropil.

Projection tracing and cell type labeling

The whole brain was cut coronally at a thickness of 80μm using a vibratome (VT1200S, Leica). 6-8 brain sections were selected per region including the Primary Motor Cortex and Primary Visual Cortex. The collected sections were placed free-floating in blocking buffer at room temperature overnight (2% Triton-X, 10% Normal Donkey Serum, 0.04% NaN_3 in 1x TBS). The following day, the brain sections were transferred to primary antibody solution (1:1000 anti-PV: guinea pig, AB_572259 ImmunoStar; 1:200 anti-SST: rat, MAB354, Millipore Sigma, 1:200 anti-VIP: rabbit, AB_572270, ImmunoStar in blocking buffer) and incubated 6-8h in room temperature, followed by 2 nights in a cold room, followed by 6-8h at room temperature. The sections were washed 3 times for 3 minutes followed by 3 times for 15 minutes each in blocking buffer. The brain sections were then transferred to secondary antibody solution at a concentration of 1:1000 antibody to blocking buffer. (anti-Guinea Pig DyLight 405: Donkey, 706-475-148, Jackson ImmunoResearch; anti-Rat Alexa Fluor 647: Donkey, 712-605-153, Jackson ImmunoResearch; anti-Rabbit Alexa Fluor 488: Donkey, 711-545-152, Jackson ImmunoResearch) and incubated overnight at room temperature. The sections were again washed 3 times for 3 minutes followed by 3 times for 15 minutes each in blocking buffer. Finally, the sections were washed with 1× TBS and 1× PBS for 10 min each. All washes and incubation periods were performed on a shaker. Vibratome cut sections were mounted on glass slides (Superfrost Plus, Thermo Scientific). All sections were coverslipped (Thermo Scientific) using 50:50 glycerol:1× PBS.

Single tile images were acquired using a Leica TCS SP8 confocal microscope using a 10X / 0.40 NA objective. The XY image dimensions were 1551 by 1551μm with a Z range of 15 to 20 μm across 5 Z planes. For analysis, the images were maximum projected along the Z planes for each channel. The cell ROIs were manually labelled in the tdTomato channel using FIJI. To determine overlap of tdTomato cells with interneuron cell types, mean intensity measurements were made of the tdTomato-based ROIs across each of the channels (PV/SST/VIP). If the mean intensity of an ROI was 2 standard deviations above the pooled ROI average intensity of the respective channel (PV/SST/VIP), the cell was identified as a positive overlap. A positive overlap indicates that the identity of the tdTomato cell is PV, SST, or VIP respectively. The ROI measurements were pooled by animal and thus the threshold for interneuron (PV/SST/VIP) identification was determined per animal. The overlap/cell identity results are manually inspected for quality control.

Behavioral setup

Mice were head-fixed on a behavioral rig, placed on top of a running wheel (Bio-Serv) attached to a rotary encoder (LPD3806-600BM-G5-24C). A monitor (15 by 9cm, 800 by 600-pixel resolution) was placed perpendicularly 14cm in front of the eye contralateral to the imaged hemisphere. Drifting gratings (0.04 cycles per degree, 2 cycles per second, 8 directions) or natural movies were displayed to the mouse at three contrasts (4%, 16%, 64%), while the mouse was free to run on the running wheel. In some imaging sessions, a mild air-puff was delivered 2 seconds before the onset of 90° gratings or movie number 1, on alternating blocks of stimuli presentations. The delivery of an air puff was through a small tube 3 cm away from the whisker pad and eye ipsilateral to the imaged hemisphere (compressed air at 40 psi for 0.3 s) and was controlled through a solenoid valve (003-0137-900, Parker) and microcontroller board (Arduino UNO).

Timing of stimuli and air puff as well as collection of running speed was controlled with a custom MATLAB script, with visual stimuli being generated through Psychtoolbox, and running wheel rotation and air-puff valve openings being logged through two microcontroller boards (Arduino UNO). The face and pupil of the mouse was recorded with a Thorlabs CMOS camera (CS165MU - Zelux®, Thorlabs) with an infrared filtered lens (#59-871, 25mm C Series Fixed Focal Length Lens, Edmund Optics). Infrared illumination at 780nm was provided by a light-emitting diode array light source (Thorlabs LIU780A). Video acquisition of the face was performed at 20 Hz by a custom MATLAB script. The presentation of visual stimuli, pupil imaging, and calcium imaging were aligned via 5-volt square wave pulses generated by the computer controlling stimulus timing via a National Instruments data acquisition device (National Instruments BNC-2110 Terminal Block).

Two-photon imaging parameters

Two weeks after the mice were implanted with a cranial window, the fluorescent signal (axon-GCaMP6s or GCaMP7f) was imaged using resonant-galvo scanning with a Prairie Ultima IV two-photon microscope system. A XLUMPlanFL N 20× 1.00NA (Olympus) objective was used for single plane imaging with a field of view size of 588x588μm. Axonal activity was recoded at a 2x digital zoom and somatic activity was recorded with either 1.5x or 1x digital zoom, at a 512x512 pixel resolution. Two-photon excitation of GCaMP at a wavelength of 920 nm was provided by a tunable laser (Insight X3+, Spectra-Physics). Power at the objective ranged from 10 to 30 mW depending on depth and expression levels. Images were acquired at a frequency of 30.2Hz and every 4 frames were averaged for axonal imaging and every other frame for somatic imaging. Axonal activity recording was performed on a new field of view every day at a depth ranging from 10-150um from the brain surface. Somatic activity imaging was performed on the same set of neurons across two days (one saline day, and one CNO day).

Preprocessing of behavioral and imaging data

Pupil size

Videos captured of the face of the mouse was used to post-hoc extract 8 xy-coordinates surrounding the pupil using Deep Lab Cut.[57] ~500 frames were manually labeled (~20 frames/ video) and a resnet v1 50-based convolutional neural network was trained to predict the location of the 8 markers for 50,000 iterations. A new network was trained for each experimental cohort. Once the network was trained, it was used to place coordinates on unlabeled frames / videos and the quality of the labeling was manually evaluated by observing at least 10 labeled videos. The distance of each xy-coordinate to the corresponding xy-coordinate across the pupil was calculated, corresponding to the diameter of the pupil in pixels. This was repeated for the 4 pairs of coordinates labeled and averaged to provide a more stable and representable pupil diameter across the entire session. Any major outliers in label position (a label suddenly jumping away from the eye) was removed post-hoc by removing values above the 99th percentile of pupil values.

Face movements

The same videos used to extract pupil diameter information was used to extract face movement information. The videos were processed using FaceMap[58] extracting the absolute motion energy (abs(current_frame - previous_frame)) for the entire face of the mouse.

Axonal imaging

2-photon axonal activity imaging was performed at a framerate of 30.2 Hz and every 4 frames was averaged resulting in a framerate of 7.55 Hz. The tiff timeseries was motion corrected twice using the Template Matching plugin in Fiji (ImageJ). The imaging sessions were motion corrected a third time in Suite2p[26] and ROIs extracted.

The detection of axonal ROIs in Suite2p was without boundaries of size and manually curated afterwards. The fluorescence signal from the ROI was taken as $F_{ROI} = F_{ROIraw} - 0.8 * F_{neuropil}$. For computing ΔF/F ($\Delta F/F = (F - F_0)/F_0$) for each ROI, F_0 was either calculated as the mean value of F over the entire session for analysis of continuous variables, (e.g., running, face movements) or the mean value of the immediate baseline (1-2 sec) preceding the onset of an event, for analysis regarding discrete events (e.g., a visual stimulus).

In order to cluster boutons that may potentially be from the same neuron, we performed pairwise correlations between every ROI. We then performed hierarchical clustering based on these pairwise temporal correlations. The number of clusters was determined empirically for each session by iteratively testing multiple distance thresholds to satisfy a cluster correlation threshold where 1) The minimum within/intercluster correlation was >0.2 and 2) at least to times of that of the 85th percentile between/inter-cluster correlation. To ensure this did not result in any false positives, 3) the same distance threshold applied to a shuffled dataset should not have any statistical difference between the between and within cluster correlations. We weighted boutons of each cluster by the signal-to-noise ratio of the ROI, taking a weighted average of fluorescence signals to represent bouton clusters (referred to as axons throughout the paper).

Somatic imaging

2-photon somatic activity imaging was performed at a framerate of 30.2 Hz and every other frame was averaged resulting in a framerate of 15.1 Hz. Motion correction was performed within Suite2p and ROI detection was performed without size constraints and manually curated. Somas imaged across days were identified using ROIMatchPub and manually confirmed. The fluorescence signal from each soma was taken as $F_{ROI} = F_{ROIraw} - 0.8 * F_{neuropil}$. For computing ΔF/F ($\Delta F/F = (F - F_0)/F_0$) for each soma, F_0 was either calculated as the mean value of F over the entire session for analysis of continuous variables, (e.g., running, face movements) or the mean value of the immediate baseline (1-2 sec) preceding the onset of an event, for analysis regarding discrete events (e.g., a visual stimulus).

DREADD manipulations

In the chemogenetic DREADD experiments, mice were injected with 1mg/kg Clozapine-N-oxide intraperitoneal (i.p.) or with saline (0.9% NaCl) of the same volume of the drug administration. Mice were imaged at least 30min after the i.p. injection. Chemogenetic constructs were only expressed unilaterally in these experiments.

QUANTIFICATION AND STATISTICAL ANALYSIS

Analysis

Analysis of visual responses in axons or somas

To determine if an axon or soma was visually responsive, we compared the mean value of activity 1 second pre-stimulus with the mean activity during stimulus presentation (1 second for gratings, 2 seconds for movies). A paired t-test was then performed between pre and post responses (at 3 contrasts, 10 trials/values for each contrast) for each direction of grating or individual movie. Axons or somas with a $p\text{-value} < 0.00625$ for one or several directions of drifting grating or with a $p\text{-value} < 0.01$ for one or several movies were considered visually responsive. If an axon or soma was significantly responsive to multiple directions or movies, the direction or movie with the highest response amplitude was considered the preferred stimulus.

To compare single-cell visual responses in the presence or absence of PFC modulation, only neurons that were tracked across days were used (matched neurons). From the population of matched neurons, only neurons that kept their visual responsiveness and at least one preferred direction/movie across imaging day were kept for further comparative analysis.

Orientation tuning curves of matched neurons were created by identifying the preferred stimulus of a neuron on the saline day (highest amplitude of response), and aligning the activity from the CNO day to the same preferred direction. Response amplitude for each direction was the mean ΔF/F activity during visual stimulus presentation, averaged across all presentations of that direction.

The direction selectivity index was also computed as:

$$DSI = \frac{\left(R_{pref} - R_{null}\right)}{\left(R_{pref}\right)}$$

Where the R_{pref} and R_{null} are responses at the preferred (pref) and preferred + 180° (null) orientation respectively.

Behavioral state

For a visual response to be classified as occurring during a discrete behavioral state the mouse needed to be moving/aroused above the set threshold (defined for each panel in the figure ledged) for the entire trial, 1 sec before, during visual stimuli, and 1 second after visual stimuli.

Decoding stimulus identity and contrast

We built linear support vector machine (SVM) classifiers using the *fitceco* function in MATLAB. All population decoding was performed for each session. For the training and testing dataset, the number of trials in each condition (eight directions and three contrasts) was matched to prevent bias for training classifiers. We used three-fold cross-validation by leaving a 33% subset of trials for prediction to avoid overfitting. This procedure was repeated 50 times. To avoid overestimating the weights, we applied Lasso regularization using a *templateLinear* function in MATLAB. Hyperparameter such as λ regularization weight was determined by optimization to minimize loss of validation dataset in a grid search manner (searched range $10^{-6} - 10^{-1}$).

We used the mean ΔF/F response during stimulus presentation (1 second for gratings, 2 seconds for movies) for each individual neuron, respectively. Classifier performance on each iteration was estimated by averaging decoding accuracies across the three folds. Final decoding accuracy was determined by averaging these mean accuracies across all iterations. To obtain cross-validated single-trial accuracy values, we averaged the binary prediction accuracy of each trial across all cross-validation folds and iterations in which it was held out as part of the test set. To determine if the decoder was informative above chance, we shuffled labels for the test data and trained and tested decoder to assess the decoding accuracy.

For statistically assessment of the decoding accuracy between sessions, we trained and tested decoders using subset of population of neurons (from 10-200 neurons, at 10 neuron increments) by randomly choosing neurons in each iteration. Difference in decoding accuracy between two conditions (saline and CNO) were evaluated in multiple ways. First, by performing a 2-way ANCOVA to examine the effects of subset (number of neurons) and experimental condition (saline/CNO) on the accuracy of decoding. The model included interaction terms to explore if the effect of subset size on accuracy varies by group and data/shuffled data. p-values noted in the figures are from the variability in accuracy explained by group (saline vs. CNO). Second, by performing a paired t-test on the average accuracy per subset across paired recording sessions (imaging field of views). Lastly, by computing the difference in decoding accuracy for each group and subset between the data and the shuffled data, and thereafter performing a paired t-test of the differences in delta decoding accuracy between paired recording sessions and subset size.

Generalized Linear Model (GLM) of soma and axonal activity

To identify the visual information and behavioral variables of soma and axon, we used a GLM with linear (identity) link function. In this model, the soma and axonal activity is described as a linear sum of visual and behavioral predictors aligned to each event. The predicted soma or axonal activity $r_n(t)$ for a soma or axon n is described as

$$r_n(t) = \sum_{c} \sum_{t_s \in S_c} \beta_{c,n}^{t_s} x_c(t - t_s) + \sum_{b} \beta_{b,n} x_b(t) + \beta_{p,n} x_p + \varepsilon$$

where c represents the direction and contrast of visual stimulus (eight direction x three contrasts), b represents the behavioral variables (pupil diameters, face velocity, running speed, binarized pupil diameters, and binarized running speed), p represents the air puff, S_c represents the set of times to cover each predictor window. $\beta_{c,n}, \beta_{b,n}, \beta_{p,n}$ represents the weights of visual stimulus, behavioral variables, and air puff for soma or axon n. The visual stimulus predictors cover the window -1-3 s from stimulus onset. x_c, x_b, x_p represents the visual stimulus, behavioral variable, and air puff predictors. Each predictor coded as "1" or "0" except for behavioral variables. Behavioral variable predictors are the continuous behavioral event variables such as pupil diameter. ε is the model bias (intercept). The values for the behavioral variables were z-scored. The soma or axonal activity was binned into 0.2seconds.

To estimate the optimal weights for each soma or axonal activity without overfitting, the *lassoglm* function in MATLAB with tenfold cross-validation of the training set was used with a lasso regularization according to the value of a selected parameter λ, which represents regularization coefficients. The value of λ in the lassoglm function was set to be 10^{-3}. Model performance was assessed for the test dataset by quantifying explained variance (R^2).

To determine the contribution of each variable to soma or axonal activity, we fitted the model using full predictors (full model) and predictors in which the target predictor is set to zero within whole-time points (partial model) and calculated the explained variance ($R^2_{full}, R^2_{partial}$) of the full and partial model. We defined relative contribution of each variable to soma or axonal activity by determining how much the performance of the partial model declined compared to full model.

In this study, proportional contribution of variable *v* is calculated as proportion of all variable's contribution to the model:

$$\textit{proportional contribution} = \left(R^2_{full,v} - R^2_{partial,v}\right) \Big/ \sum \left(R^2_{full} - R^2_{partial}\right)$$

where $R^2_{partial,v}$ represents explained variance of partial model of *v*th variable. Negative relative contributions were set to zero (this means partial model performed better than full model).

The proportion of axons or somas with a significant contribution of the variance explained by variable *v* was calculated by performing a t-test between the R^2_{full}, and $R^2_{partial}$ across the 10-fold cross validation, correcting for multiple comparisons with Bonferroni-Holm correction.

Statistical Methods

Statistical methods and parameters for each analysis/figure panel are noted in the figure legends. Statistical analysis was carried out in Python 3.8.8 using the sklearn and scipy libraries.